Geochemistry, Geophysics, Geosystems

RESEARCH ARTICLE
10.1029/2020GC009316

Key Points:

- Isotropic onshore-offshore teleseismic body wave tomography of the Cascadia subduction zone; Updated P- and new S-wave models
- Forward modeling quantifies the effects of crustal thickness, elevation, sediments, and velocity variations on the shore-crossing dataset
- We explore the impacts of inversion strategy choices, identify imaging artifacts, and outline a preferred methodology

Supporting Information:

- Supporting information S1

Correspondence to:
M. Bodmer,
mbodmer@uoregon.edu

Citation:
Bodmer, M., Toomey, D. R., VanderBeek, B., Hooft, E. E., & Byrnes, J. S. (2020). Body wave tomography of the Cascadia subduction zone and Juan de Fuca plate system: Identifying challenges and solutions for shore-crossing data. *Geochemistry, Geophysics, Geosystems*, *21*, e2020GC009316. https://doi.org/10.1029/2020GC009316

Received 28 JUL 2020
Accepted 16 NOV 2020

Body Wave Tomography of the Cascadia Subduction Zone and Juan de Fuca Plate System: Identifying Challenges and Solutions for Shore-Crossing Data

M. Bodmer[1], D. R. Toomey[1], B. VanderBeek[2], E. E. Hooft[1], and J. S. Byrnes[3]

[1]Department of Earth Sciences, University of Oregon, Eugene, OR, USA, [2]Department of Geosciences, Università di Padova, Padua, Italy, [3]Department of Earth and Environmental Sciences, University of Minnesota, Minneapolis, MN, USA

Abstract Recent seismic results from the Cascadia Initiative indicate that heterogeneity in the oceanic asthenosphere affects subduction dynamics. Accurate characterization of the oceanic upper mantle is thus necessary to fully understand subduction processes, including the behavioral segmentation of the megathrust. A key challenge is integrating onshore and offshore datasets, which span large variations in near-surface features that teleseismic body wave tomography is ill-posed to resolve. Here, we perform a series of P and S forward modeling predictions to better understand the relative contribution of elevation, crustal thickness, offshore sedimentation, and near-surface velocity structure to teleseismic delay times. Crustal thickness and elevation variations dominate the signal, contributing ~1 s of delay time difference for P-waves (roughly double for S). We test several inversion strategies to account for near-surface features, identifying potential artifacts and causes of imaging errors. Undamped station statics are found to absorb mantle structures and introduce low-velocity artifacts beneath the forearc. Our preferred inversion strategy utilizes a three-dimensional starting model (including elevation) of the upper 50 km and heavily damped station statics, which we find leads to better resolution of mantle structure, particularly at asthenospheric depths. These insights guide inversions of observed delay times from the Cascadia subduction zone and Juan de Fuca plate system. We present a new onshore-offshore S model and an updated P model. Major features are common to both models, including localized subslab low-velocity anomalies, along-strike variations in slab structure, and offshore heterogeneity, while regional differences may reflect changes in Vp/Vs.

1. Introduction

Subduction zones are regions where oceanic lithosphere is recycled into the mantle, the largest earthquakes and tsunamis are generated, continental crust is built through accretion and arc magmatism, and volatiles are circulated, key to the petrogenesis, transport, storage, and eruption of magmas (Stern, 2002). Fundamentally, subduction processes are dependent upon properties of both the incoming oceanic lithosphere, the overriding plate, and the surrounding convecting mantle. Worldwide, subduction systems have been studied extensively with seismic methods, producing images of the convergent margin structure, characterizing and cataloging regional seismicity, and developing hazard assessments. Most seismic datasets are inherently limited, however, comprised of only land-based observations and lacking comparable data from the offshore oceanic plate. Those studies capable of obtaining coincident, shore-crossing data are often limited in their spatial scope (e.g., Parsons et al., 2005; Trehu et al., 1994). Only recently, through experiments such as the community-driven Cascadia Initiative (CI), are we able to collect dense, amphibious seismic data spanning large portions of a subduction margin (Toomey et al., 2014).

A key takeaway from the CI is that characterizing the structure of oceanic asthenosphere is critical to understanding subduction dynamics, yet, relatively few studies have investigated joint onshore-offshore structure (Bodmer et al., 2018; Gao, 2018; Hawley & Allen, 2019; Hawley et al., 2016; Janiszewski et al., 2019) and many of these provide conflicting results. Notably, studies of teleseismic P-wave velocity structure vary significantly in both methodology and interpretation. Hawley et al. (2016) image a margin-wide, low-velocity anomaly beneath the subducting slab using a one-dimensional (1D) flat-earth model and station static corrections to account for variations in near-surface structure. Conversely, Bodmer et al. (2018) image

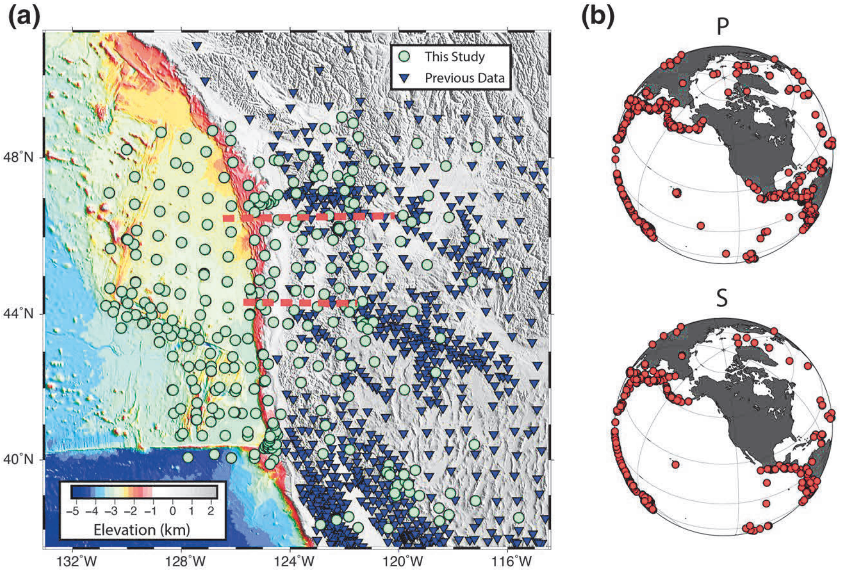

Figure 1. a) Distribution of seismic stations used in this study overlaying an elevation map of the Cascadia subduction zone. Inverted triangles represent stations with delay time measurements taken from Schmandt and Humphreys (2010a). Green circles represent stations with data processed for this study. Our dataset is a combination of these, where there is some overlap in station locations onshore. (b) Event distribution for the P and S delay time datasets. Red dashed lines represent the general location of the two shore-crossing 2D refraction lines evaluated in Figure 3.

localized low-velocities beneath the slab in the north and south using *a priori* three-dimensional (3D) starting models that include elevation to account for near-surface structure. Understanding how these methodological choices influence the tomographic results is important because there is pronounced variability in along strike subduction behavior (e.g., plate locking, tremor density, long-term uplift rates, and seismicity; Bodmer et al., 2020; Brudzinski & Allen, 2007; McCrory et al., 2012; Schmalzle et al., 2014), and it is still unknown to what extent the dynamics of the oceanic asthenosphere influence these processes.

Amphibious arrays (onshore-offshore) offer significant advances to our understanding of subduction zones but introduce complications due to differences in composition, structure, and relief across the margin. This is especially problematic in teleseismic body wave tomography, which is poorly equipped to resolve heterogeneity in the near-surface (<50 km from the surface). These near-surface onshore-offshore variations impact seismic travel times, obscuring the underlying structure. Addressing these complexities is imperative to the accurate interpretation of seismic images.

Here, we investigate the P and S velocity structure of the Cascadia subduction zone (CSZ) using amphibious teleseismic broadband data. Through a series of synthetic tests, we explore the impact of near-surface structure on the observed delay times and tomographic results. We develop a strategy to account for the near-surface structure and apply it to the CSZ dataset. We then present a new S-wave velocity model and an updated P-wave velocity model of isotropic structure. Our results show consistent first-order heterogeneity in the oceanic asthenosphere, segmentation of velocity anomalies beneath the slab, and second-order differences between P and S that may reflect heterogeneity in regional Vp/Vs.

2. Tectonic Setting

The CSZ consists of the Juan de Fuca (JdF) plate, a warm, young, and relatively small oceanic plate, which is subducting beneath the western portion of the North American plate (Figure 1a). The current rate of convergence is ~45 mm/yr. The JdF plate is a remnant of the ancient Farallon plate, which was gradually consumed by subduction and fragmented into successively smaller plates (Stock & Lee, 1994). At the southern edge of the CSZ is the Mendocino triple junction, currently migrating northward at a rate of 40 mm/yr

(Atwater, 1970; Furlong & Schwartz, 2004), marking the northern extent of the San Andreas fault. Two first-order ridge segments define the western boundary of the JdF plate, the JdF Ridge to the north and the Gorda Ridge to the south. The ridge system is currently migrating to the NW at a rate of 25 mm/yr (Small & Danyushevsky, 2003) and has recently undergone a clockwise rotation and reorganization in the last 7 My (Riddihough, 1984). During this time the relatively young Blanco transform formed (Atwater & Stock, 1998) and the Explorer microplate detached (~4 Ma; Riddihough, 1984).

The southernmost section of the JdF plate is the Gorda deformation zone (GDZ; Wilson, 1989). This region is typified by diffuse plate deformation, which can be seen in the bending of magnetic anomalies, pervasive left-lateral strike-slip faulting, and abundant shallow seismicity (Chaytor et al., 2004; Wilson, 1986). Spreading rates along the Gorda ridge decrease southward from 55 mm/yr in northern Gorda to 23 mm/yr near the Mendocino transform (Riddihough, 1980). The orientation of the Mendocino transform is rotated counter-clockwise from Pacific/JdF relative plate motion by ~20°. The Pacific plate's evolving influence on the local stress field puts the Gorda into N-S compression and facilitates internal deformation (Chaytor et al., 2004; Wada et al., 2010).

Previous mantle tomography studies of the western United States consistently image a dipping high-velocity feature beneath the western United States, interpreted as the JdF slab subducting into a relatively low-velocity upper mantle (Becker, 2012). Schmandt and Humphreys (2010a) trace the slab to a depth of 350 km in southern Cascadia, accounting for 15 Ma of subduction. A robust feature of these studies are along-strike amplitude variations of the slab at depths below ~150 km, referred to as the slab "hole" (Obrebski et al., 2010; Roth et al., 2008; Tian & Zhao, 2012). High-velocity anomalies tend to decrease in amplitude beneath Oregon. Some have attributed this to a slab-plume interaction (Geist & Richards, 1993; Obrebski et al., 2010) and/or a tear in the slab (Hawley & Allen, 2019), while others have suggested that it is an imaging artifact (Roth et al., 2008). If the slab is nonexistent in this region, that has implications for dynamic models relying on slab rollback to drive mantle circulation (Long, 2016). Beneath 440 km depth, many researchers image independent high-velocity anomalies interpreted to be older, fragmented sections of the Farallon plate (e.g., Obrebski et al., 2010; Schmandt & Humphreys, 2010b; Sigloch et al., 2008).

Though the margin is relatively short (~1,200 km), along-strike variations exist in megathrust behavior (Brudzinski & Allen, 2007; McCrory et al., 2012; Schmalzle et al., 2014; Wells et al., 2017), forearc kinematics and structure (Bodmer et al., 2020; Burgette et al., 2009; Kelsey et al., 1994; Leonard et al., 2010; Schmalzle et al., 2014), and mantle structure (Bodmer et al., 2018; Chen et al., 2015). However, the underlying mechanisms giving rise to these variations and how they may be interrelated is still debated. Many studies focus on properties of the overriding crust, incoming oceanic crust, or properties along the plate interface to explain along-strike segmentation in megathrust processes (Audet et al., 2009; Brudzinski & Allen, 2007; Cloos, 1992; Delph et al., 2018; Littel et al., 2018; Ruff, 1989). However, there is evidence that heterogeneity within the oceanic asthenosphere plays an important role in subduction phenomena (Bodmer et al, 2018, 2020; Hawley & Allen, 2019). Nearby hotspots and/or local flow dynamics may emplace buoyant mantle beneath the subducting slab (Bodmer et al., 2018; Gao, 2018; Portner et al., 2017), creating localized anomalies in the subslab. Conversely, a thin buoyant layer at the base of the lithosphere may be pooling beneath the downgoing slab (Hawley et al., 2016), a phenomena which would be pervasive among subduction zones.

Results from the CI show that the oceanic asthenosphere is much more heterogeneous than previously assumed. At the JdF Ridge, there is evidence for dynamic upwelling and ridge asymmetry, suggesting incipient deep (~200 km) melting and an associated mantle downwelling beneath the JdF plate interior (Bell et al., 2016; Byrnes et al., 2017; Eilon & Abers, 2017; Rychert et al., 2018). Beneath the GDZ, several studies image low velocities broadly distributed beneath the plate with an unclear relationship to the Gorda spreading center (Bell et al., 2016; Bodmer et al., 2018; Byrnes et al., 2017). Mantle anisotropy is also heterogeneous both laterally, reflecting distinct tectonic regimes (Bodmer et al., 2015; Martin-Short et al., 2015), and in depth, reflecting the interplay of plate evolution and asthenospheric flow (Eilon & Forsyth, 2020; VanderBeek & Toomey, 2017, 2019).

3. Body Wave Delay Time Data

Seismic stations used in this study span the Cascadia margin and the entire JdF plate system. Onshore instrumentation is largely provided by the Transportable Array (TA), which deployed seismometers across the United States at a ~70 km spacing, starting in 2007 and progressing eastward.

Table 1
Comparison of Various Forward and Inverse Models

Model	RMS (Vp)[a]	Variance reduction (Vp)[a]	RMS (Vs)[a]	Variance reduction (Vs)[a]
G18	0.44 s	*−38%*	0.86 s	*−3%*
B16/D18	0.38 s	56%	0.64 s	19%
B16/SL14	0.36 s	58%	0.61 s	37%
FakeCrust		35%		*−17%*
Elevation		34%		15%

Synthetic inversion results

Model	RMS (Vp)	Variance reduction (Vp)	Station static (Vp)	RMS (Vs)	Variance reduction (Vs)	Station static (Vs)
Slab only[b]	0.25 s	-	-	0.31 s	-	-
Initial misfit	0.40 s	-	-	0.74 s	-	-
1D starting model	0.29 s	48%	-	0.40 s	71%	-
Undamped station statics	0.28 s	53%	0.28 s	0.37 s	75%	0.55 s
Damped station statics	0.28 s	53%	0.21 s	0.37 s	75%	0.30 s
3D starting model	0.28 s	50%	-	0.40 s	72%	-
Heavily damped 3D starting model	0.27 s	53%	0.09 s	0.37 s	74%	0.14 s

Observed data inversion results

Model	RMS (Vp)	Variance reduction (Vp)	Station static (Vp)	RMS (Vs)	Variance reduction (Vs)	Station static (Vs)
Initial misfit	0.46 s	-	-	1.13 s	-	-
1D starting model	0.25 s	71%	-	0.72 s	60%	-
Undamped station statics	0.21 s	78%	0.53 s	0.67 s	65%	1.13 s
Damped station statics	0.21 s	78%	0.43 s	0.67 s	64%	0.60
3D starting model	0.25 s	70%	-	0.72 s	60%	-
Heavily damped 3D starting model	0.23 s	75%	0.10 s	0.69 s	63%	0.13 s

Abbreviation: RMS, root mean square.

[a] RMS and variance reductions here refer to station-averaged delay times. [b] Slab Only model does not include FakeCrust in the synthetic delays.

From 2011 to 2015, ocean-bottom seismometers were deployed on the JdF plate system offshore, with permanent stations and TA redeployments tying it to the existing data (Toomey et al., 2014).

Our study combines P- and S-wave delay time measurements from the CI with previously reported teleseismic delay time data from onshore studies. Legacy onshore delay time data comes from Schmandt and Humphreys (2010a), which has been used in several follow-up studies (Schmandt et al., 2012; Schmandt & Humphreys, 2011; Schmandt & Lin, 2014). We use a subset of their data that covers the geographic area of interest (see Figure 1). This onshore relative delay time dataset contains multiple phases (P, pP, PKP, S, sS, and SKS) measured at multiple frequency bands. The Schmandt and Humphreys data provide 69,907 P-wave delay times (48%, 29%, 22%, and 1% at 1, 0.5, 0.3, and 0.1 Hz center frequency, respectively) and 22,357 S-wave delay times (43%, 55%, and 2% at 0.05, 0.1, and 0.4 Hz center frequency, respectively); for additional details see Section 2 of Schmandt and Humphreys (2010a).

Shore crossing delay times used for this study come from the 4-year-long CI community experiment (Toomey et al., 2014), and separate year-long studies of the Blanco transform and the Gorda region

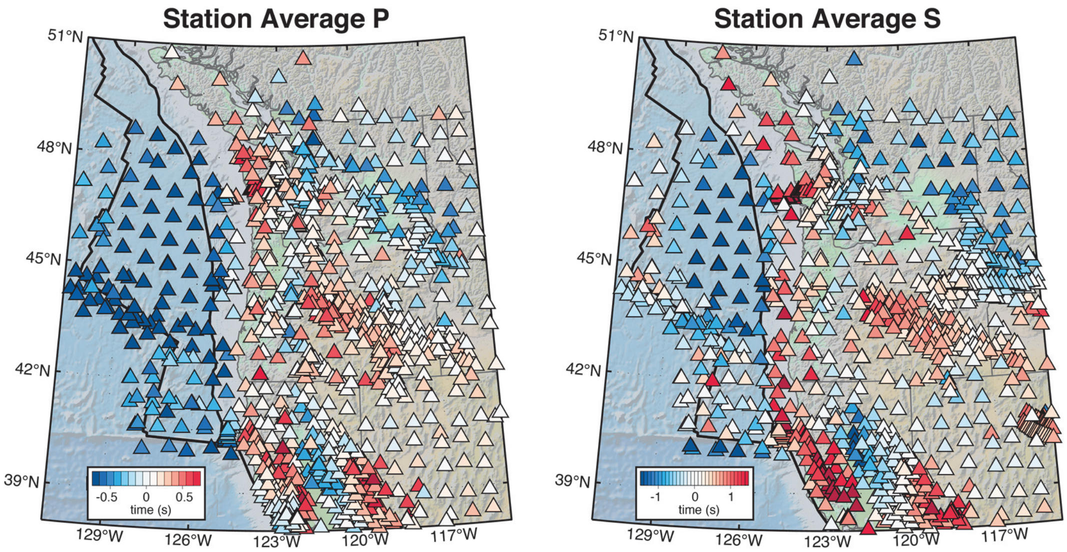

Figure 2. Average station delay times for the observed P and S datasets. Both datasets show a bimodal, onshore-offshore signal. Average station delays should be most sensitive to structure near the seismic station.

(Kuna et al., 2019). The CI amphibious array comprised 27 onshore sites and 258 ocean bottom seismometer (OBS) sites that were deployed in ∼10-month-long intervals (∼60 OBS/yr), allowing them to span the entirety of the JdF plate system, including the JdF Ridge, Gorda Ridge, Blanco transform, GDZ, and the CSZ (Figure 1a). The Blanco and Gorda experiments occurred coincident with the CI and provide an additional 30 and 24 OBSs, respectively. The shore crossing P-wave delay time dataset was first presented in Bodmer et al. (2018). In this study, we present a new S-wave relative delay time dataset.

We processed the CI waveform data as follows. Instrument response was deconvolved following the method of Haney et al. (2012) and a third-order Butterworth filter (corner frequencies of 0.0303 and 0.0833 Hz) was applied prior to measurement of delay times using cross-correlation (VanDecar & Crosson, 1990). A single, relatively low-frequency band is used for the offshore data due to high noise in the microseism band of the OBS data. Because the errors reported by the cross-correlation method are unrealistically small, the minimum uncertainty for all delay time measurements was set to 0.25 s, a conservative estimate based on analysis of synthetic cross-correlations (see supporting information of Byrnes et al., 2017). Figure S1 shows examples of teleseismic waveforms and quality control procedure are described in the supplementary text.

Altogether, our analysis uses 98,268 teleseismic P-wave delay times from 1,559 events (>M5.5) recorded at 1,076 stations (34,794 arrivals from CI), and 60,063 teleseismic S-wave delay times from 724 events recorded at 1,022 stations (37,740 arrivals from CI). Figure 1b shows the distribution of teleseismic events, with the highest contributions from Japan, South America, and Tonga. The root mean square (RMS) of all delay times is 0.46 s for P and 1.13 s for S (Table 1).

Station-averaged delay times show a clear signal that correlates with elevation (Figure 2) and variations in crustal thickness (Laske et al., 2013). In both P and S datasets, the largest signal is a bimodal response with advanced (negative) delays offshore and more positive delays onshore. The RMS of the station-averaged delay times is 0.40 s for P and 0.80 s for S. This amount of variability is comparable to that of the entire dataset, suggesting that near-surface contributions are the first-order signal reflected in the observations.

There are several additional regional-scale trends in the station-averaged delays (Figure 2). A north-south band of advanced delay times is observed in the region just west of the Cascade volcanic arc. Advanced delay times are also observed trending northwest-southeast in Washington and broadening in western Idaho. Regions of slower arrivals include central Oregon east of the Cascades, Northern California near the southern edge of subduction (Beaudoin et al., 1998), and in a N-S band along the forearc near the coastline. Offshore, advanced delay times are largest in the JdF plate interior and along the Blanco transform. Station-averaged delays become slower near the JdF Ridge and throughout the Gorda region. These offshore variations are much more pronounced in the S-wave data.

4. Tomographic Method

Our tomographic method is well-suited for amphibious data because it treats the forward problem accurately and explicitly includes prior states of knowledge, including uncertainties (e.g., Jackson, 1979; Tarantola & Valette, 1982). Simple examples of prior states of knowledge include elevation and crustal thickness, features that can vary for a given regional experiment but become much more significant when considering an array spanning the ocean-continent transition. Because teleseismic body waves are nearly vertical close to the receiver and the model node spacing is relatively large, inversions lack the resolution to capture these features. Our methodology allows us to explicitly include prior states of knowledge as *a priori* assumptions, enabling us to test many hypothetical models to better understand how variations near the surface impact the resulting images. We find this to be useful in ocean-continent subduction settings, but similar issues are likely to arise in any setting where structure near the surface changes significantly across the seismic array.

Our workflow is distinct in a number of ways: (1) the ability to define complex, 3D starting models, (2) iterative, 3D seismic ray tracing, and (3) a flexible scheme for regularizing inversions. Teleseismic body-wave studies make simplifying assumptions when calculating predicted delay times. Often, a single inversion iteration is performed on a model that assumes a flat (zero elevation), laterally homogenous earth with seismic ray paths calculated using a 1D model. Our method allows us to explicitly include elevation and iteratively ray trace through complex 3D starting models, allowing ray paths to adjust to anomalous structures. Further details of our methods are presented elsewhere (Bezada et al., 2013; Byrnes et al., 2017; Hammond & Toomey, 2003; Schmandt & Humphreys, 2010b; Toomey et al., 1994).

The forward problem is parametrized in terms of slowness defined on a grid of nodes, which are sheared vertically to account for elevation (Toomey et al., 1994). Nodes may be defined at regular intervals of any spacing to adapt to model complexity, though in practice computational expense limits nodal spacing. Seismic ray tracing is performed in two parts: (1) Within the tomographic volume, ray paths and travel times are calculated using Dijkstra's algorithm (Dijkstra, 1959; Moser, 1991); and (2) outside the tomographic volume, where the structure is assumed to be radial, we used the tau-p method (Crotwell et al., 2011) with the AK135 1D velocity model (Kennett et al., 1995); see (Bezada et al., 2013) for details. The choice of a starting model influences the predicted ray paths and travel times. By using starting models that include known variations in elevation and near-surface structure we can account for features that are difficult to resolve with teleseismic body waves.

The inverse problem is solved by minimizing the prediction error, a penalty function applied to the Euclidean size of the model perturbation vector, and vertical and horizontal roughness via a smoothing operator applied to the slowness perturbational model (see Toomey et al., 1994 for details). The model perturbation vector includes slowness perturbations as well as event and station statics. Diagonal data and model covariance matrices, as well as smoothing constraints, are included in the inversion, which allows the user to enforce prior knowledge (e.g., Menke, 1985; Toomey et al., 1994). We use the “banana-doughnut” kernel approximation of Schmandt and Humphreys (2010b) to account for the frequency-dependent sensitivity of delay times (Dahlen et al., 2000). Multiple iterations of the forward and inverse problem are performed, and model parameters are updated in either a jumping or creeping strategy (Shaw & Orcutt, 1985). In practice, hundreds of nonlinear tomographic inversions are conducted to test hypothetical models and to understand how inversion parameters and assumptions influence the results.

In this study, a 145 × 181 × 76 grid with 10 km nodal spacing is used for the forward calculations (centered at 125°W, 45°N). A 49 × 61 × 19 perturbational slowness model is nested within the forward model with

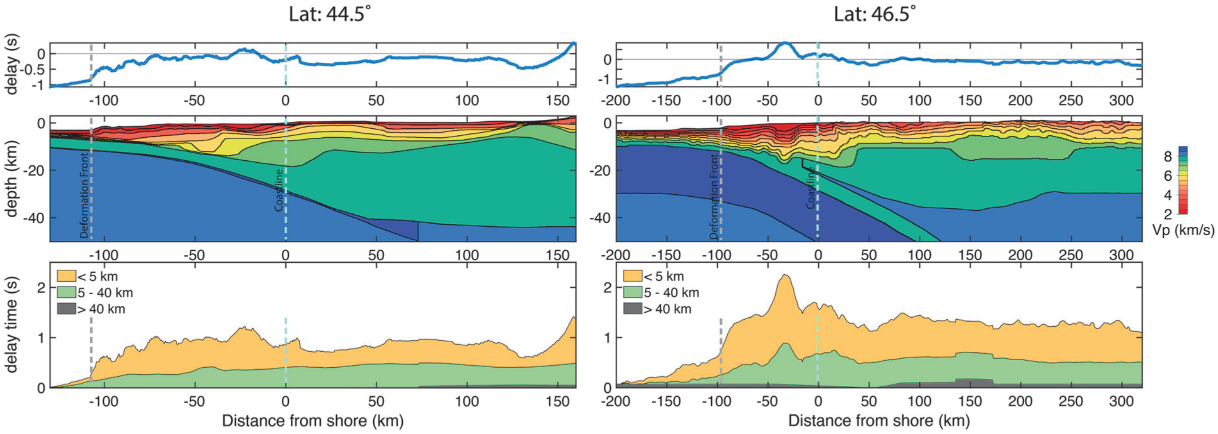

Figure 3. Forward modeling of 2D refraction profiles. Profiles are derived from shore crossing P-wave data at 44.5°N (Left; Trehu et al., 1994) and 46.5°N (Right; Parsons et al., 2005). The upper panel shows the predicted delay time anomaly relative to the AK135 prediction, along a profile assuming vertical rays. The middle panel shows the 2D P velocity models from the respective studies. The lower panel shows the relative contribution of different sections of the model to the predicted delay time. Orange signifies delay times accrued above −5 km (referenced to sea level), representing primarily changes in elevation across the margin. Green signifies delay times accrued between −5 and −40 km, representing primarily changes in crustal thickness. Black signifies delay times accrued from below −40 km. Further evaluation including a simplified model can be found in the Supplementary Info.

30 km horizontal spacing and a variable vertical spacing increasing from 30 to 60 km with depth. The fractional uncertainty of the model parameters decreases with depth below 300 km to prevent the accumulation of perturbations near the bottom of the tomographic volume. Final model weights for the damping penalty, vertical smoothness, horizontal smoothness, and station static damping are chosen through multiple inversions of real and synthetic data (for details of model parameterization see Toomey et al., 1994).

5. Forward Modeling and Inverse Strategies for Amphibious Data

We present results from forward and inverse modeling that illustrate the effects of near-surface structure (<50 km depth) on amphibious teleseismic delay times and tomographic results. In Section 5.1, we estimate the first-order contributions to teleseismic delay times for two shore-crossing P-wave refraction profiles. In Section 5.2, we predict the influence that elevation, offshore sedimentation, and crustal thickness have on teleseismic data. We then examine three potential prior models of near-surface velocity structure for the CSZ and identify a preferred starting model for use with the observed data (Section 5.3). In Section 5.4, we explore several methods used to account for near-surface structure by inverting synthetic data and comparing the results to the known model, identifying artifacts and a defining a preferred inversion strategy.

5.1. Forward Modeling of 2D Shore-Crossing Refraction Profiles

We use the results of two shore-crossing seismic refraction studies of the CSZ to quantify variations in P-wave delay times due to near-surface (<50 km depth) structure. Figure 3 shows results from Trehu et al. (1994) and Parsons et al. (2005) for refraction lines at 44.5°N and 46.5°N, respectively. Each line extends from west of the deformation front to the arc (see Figure 1). In Figure 3a, vertical travel times through the upper 50 km of each refraction profile are plotted relative to predictions through a 1D model (AK135; Kennett et al., 1995). Refraction model predictions show a ∼1 s difference in relative delay times between average onshore (∼0 s) and offshore regions (∼-1 s at the western extent). This delay time range is similar to that of the station-averaged delay time observations (for P-waves), which have a 2σ value of 0.9 s, indicating that the onshore-offshore transition is a first order signal. Local fluctuations in excess of 0.5 s (relative to AK135) are observed in geologically distinct regions, such as the continental shelf or volcanic arc, signifying a secondary signal of smaller scale heterogeneity due to local structure. Plotting the cumulative sum of vertical travel times (Figure 3c) reveals that, to a first approximation, half of the onshore-offshore signal is due to elevation (depths <5 km), while the other half is due to changes in crustal thickness (depths 5–40 km).

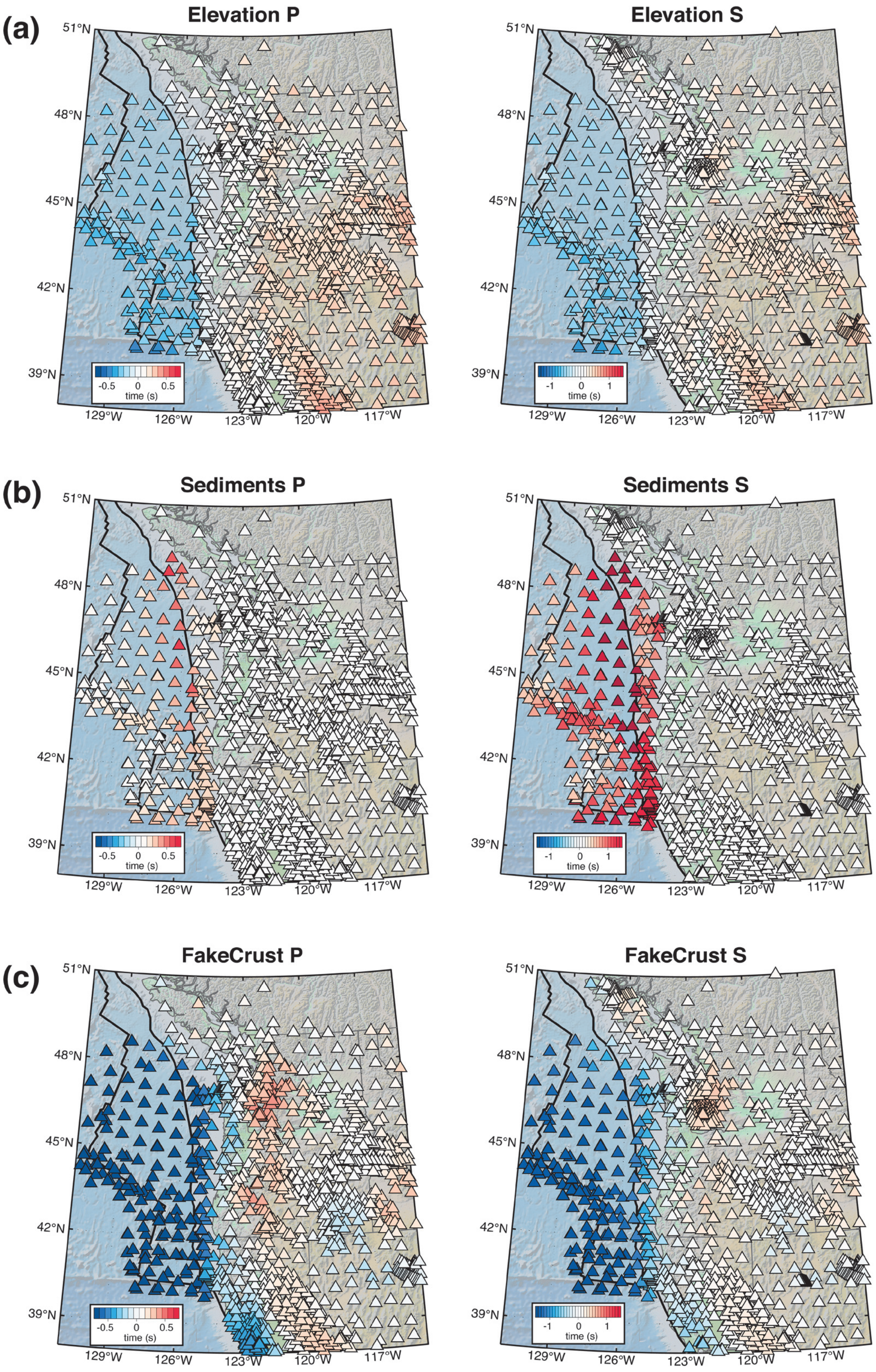

Figure 4. Forward modeling results for each station in the P and S datasets, color-coded by their delay time contribution at that site. (a) Upper panels show the delay time contributions due to elevation changes. (b) Middle panels show the delay time contributions from offshore sediments. (c) Lower panels show the delay time contributions due to velocity structure in the FakeCrust model (Section 5.3), which primarily accounts for crustal thickness variations.

These results show that structure in the upper 50 km contributes to amphibious P-wave delay time data and that the characteristic signal (~1 s of variation) is of similar order to the range of the observations. It follows that prior models of elevation, crustal thickness, or crustal velocity can be used to predict and account for the near-surface contribution to observed delay times. Since detailed refraction imaging is rarely available for the entire margin, we evaluate the magnitude of this effect by predicting vertical delay times through a simplified model using only elevation data from each refraction profile, estimating crustal thickness from isostacy, and using a simplified 2-layer crustal velocity structure (See Figure S2). These highly simplified profiles closely match our delay time predictions using the full refraction profiles, with an RMS misfit of 0.3 s (simplified prediction compared to full profile; lower panel Figure S2). We note that this comparison focuses on structure east of the deformation front, however, we expect that oceanic crustal variations are smaller generally. Detailed structural constraints, such as those from the refraction profiles, are unlikely to exist for the entire margin, however, our results suggest that even simple approximations can provide useful estimates of near-surface structure that can be built into tomographic starting models. As the availability of margin-wide constraints increases, these starting models can be further refined to improve their accuracy.

5.2. Forward Modeling of Elevation, Sediment Models, and Crustal Thickness

The greatest impact on delay times comes from elevation and crustal thickness variations (Section 5.1). We also know that offshore sediments can have a large impact on delay times, especially in S-wave data (Bell et al., 2015; Byrnes et al., 2017; Ruan et al., 2014). Here, we present forward modeling that shows the impacts of these features on the observations (Figure 4). Global models of elevation, crustal thickness, and sediment thickness are readily available, thus these features can and should be included in any shore-crossing evaluation of delay times.

Figure 4a shows the predicted variation in arrivals due to elevation changes across the margin. Travel times are calculated assuming vertical raypaths through a 1D velocity model (AK135) which is vertically sheared so that the upper interface is conformal to elevation. The lower boundary of the model is taken at a constant depth of 600 km. Travel times are presented relative to the prediction through a zero elevation 1D model (AK135). The distribution of delay times is roughly bimodal with peaks at –0.35 s and 0.1 s for P (–0.65 s and 0.2 s for S), slightly larger than predicted from 2D refraction lines (Section 5.1). The RMS of the forward modeled delays is 0.2 s for P and 0.4 s for S.

Delay times due to offshore sediments are shown in Figure 4b. Sediment thicknesses are taken from Gardner et al. (1993) and Divins (2003) and the average velocity is calculated using empirical relations from Bell et al. (2015). Where available for specific station locations, sediment thicknesses from Bell et al. (2015) are used. Sediment thickness variations can introduce delay times up to 2 s for S waves and 0.5 s for P waves.

We evaluate a simplified 3D model of the CSZ crust (FakeCrust) created using only elevation and global Moho depth estimates Figure S3. The AK135 starting model (Kennett et al., 1995) has two near-surface layers with P velocities of 5.8 km/s (0–20 km depth) and 6.5 km/s (20–35 km depth) and S velocities of 3.5 km/s (0–20 km depth) and 3.9 km/s (20–35 km depth). We vary the thickness of these layers to equal the distance between the surface elevation and the Moho depth estimated by CRUST1.0 (Laske et al., 2013; 1° lateral resolution), keeping the ratio of layer thicknesses constant. Moho depth estimates are constrained by active source experiments, receiver functions, and previously published Moho estimate maps (Laske et al., 2013; Figure S4). Travel times are calculated through this model, assuming vertical ray paths, and are used to determine the effective average slowness in the upper 50 km. This approach is necessary since the 10-km grid used for 3D ray tracing cannot exactly reproduce crustal thickness variations, resulting in a velocity model that is aphysical but produces the expected travel time estimate.

Figure 4c shows delay times through the FakeCrust model relative to the AK135 prediction, excluding elevation to isolate the crustal thickness contribution. The benefit of this type of model is that it is available for any subduction zone and focuses on the first-order influence of crustal thickness. The offshore region is largely homogenous, grading into increasingly delayed arrivals onshore with maxima occurring beneath the volcanic arc. The distribution of delay times is roughly bimodal with peaks at −1 s and 0 s for P (−1.4 s and 0.1 s for S), slightly larger than predicted from 2D refraction lines (Section 5.1). The RMS of the forward modeled delays is 0.4 s for P and 0.6 s for S.

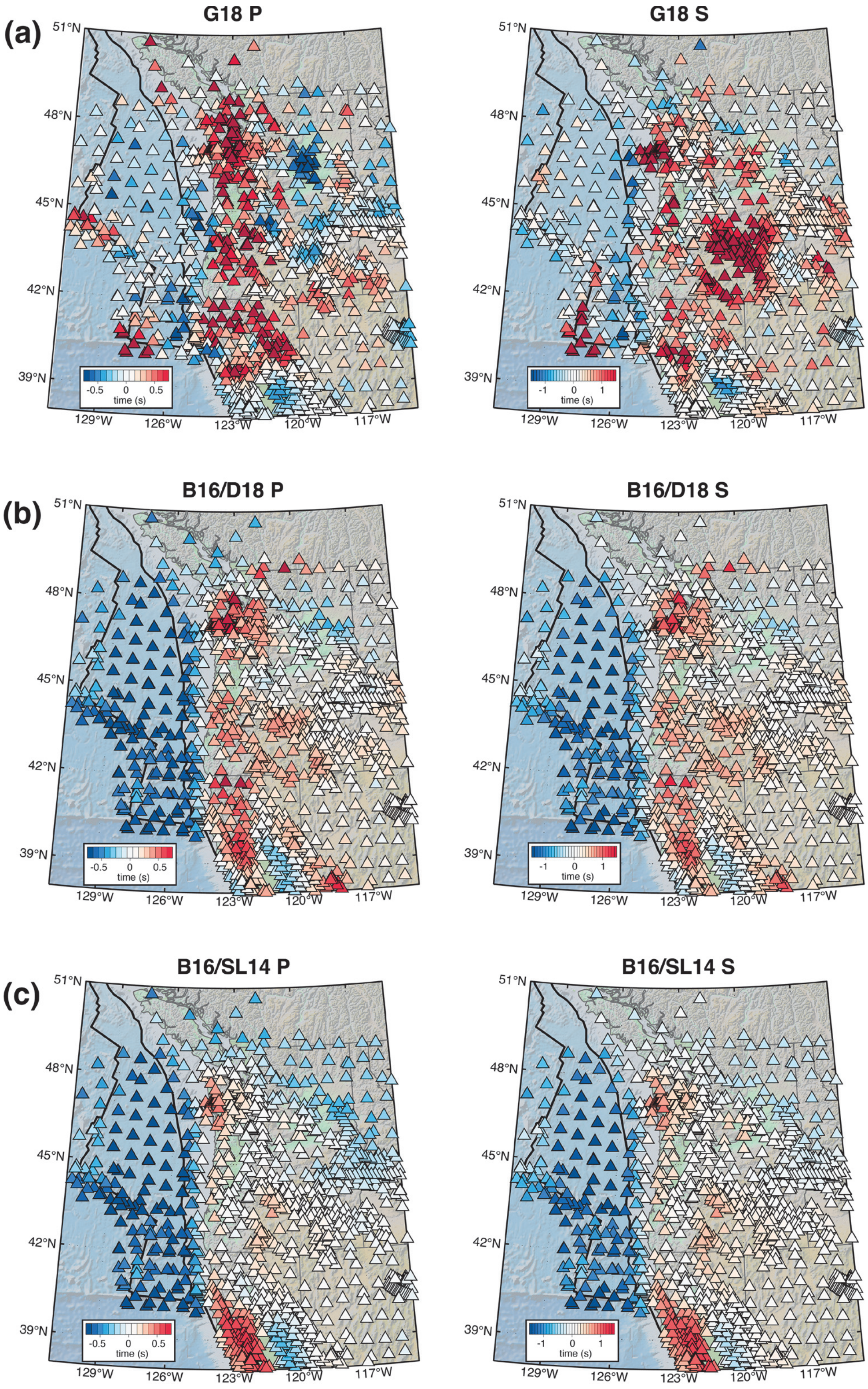

Figure 5. Forward modeling results for three 3D P and S velocity models of Cascadia. Stations are color-coded by the estimated delay time contribution at that site. (a) Upper panels show results from the Gao (2018) model (G18). (b) Middle panels show results from the hybrid model B16/D18 that blends the offshore model of Bell et al. (2016) with the onshore model of Delph et al. (2018). (c) Lower panels show results from the hybrid model B16/SL14 that blends the offshore model of Bell et al. (2016) with the onshore model of Schmandt and Lin (2014).

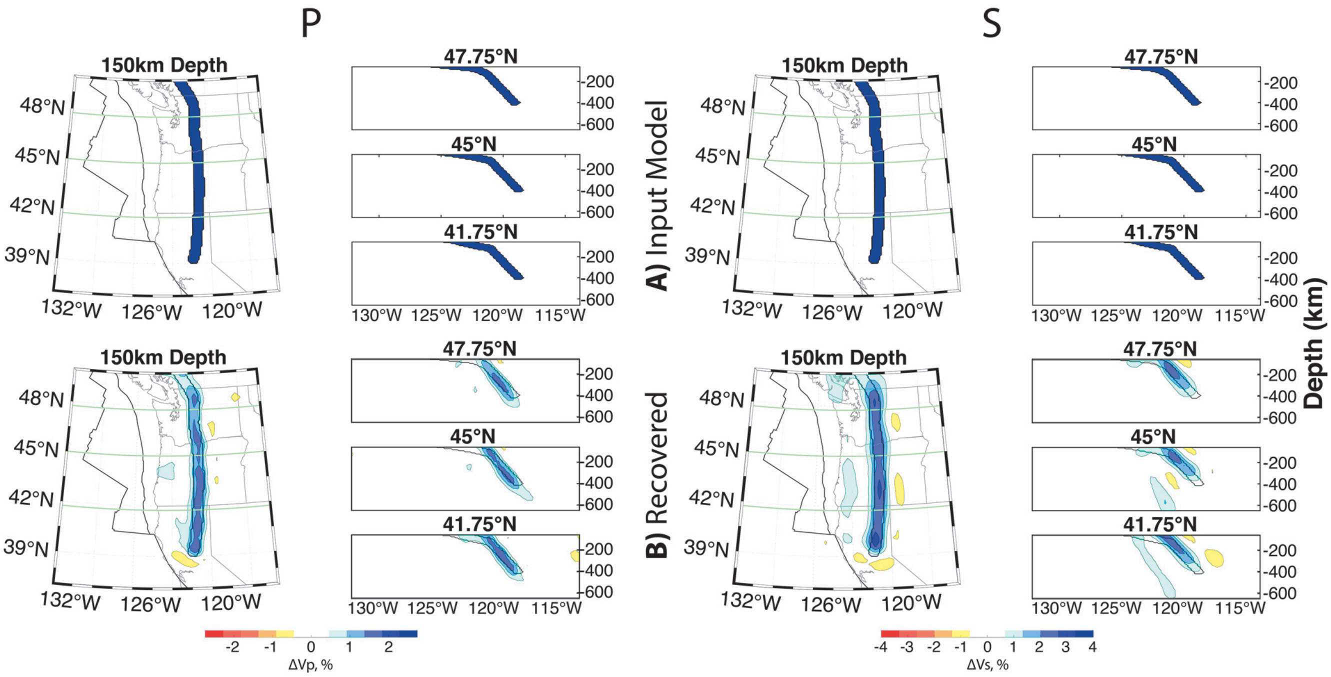

Figure 6. A) Upper panels show the synthetic input model which includes a high-velocity anomaly mantle target representing the subducting Juan de Fuca slab. The synthetic slab (50 km thick) is defined between 50 and 440 km as 2% and 4% anomalies for P and S, respectively. B) Bottom panels show results from inversions of the synthetic data for this target structure only (no structure in the upper 50 km). The gray contours indicate the location of the slab in the synthetic model.

We use the FakeCrust model in the synthetic inversions (Section 5.4) since it eliminates biases inherited from any published velocity model of the area (Section 5.3). Though the Moho depth estimates used are constrained by previous seismic results, FakeCrust is largely generic and could be further generalized by using elevation data to estimate a crustal thickness model, but the results are similar. Because FakeCrust depends only on first order data constraints (elevation and crustal thickness), the synthetic inversion results are applicable to other onshore-offshore systems. We note that the FakeCrust model does not give any special consideration to the forearc, which is expected to have anomalous structure, and thus provides a test of the onshore-offshore transition in elevation and crustal thickness. When considering the observed delay time data and inversions we will use more specific, detailed models of the CSZ (Section 6).

5.3. Forward Modeling of Existing 3D Near-Surface Velocity Models

We investigate the predicted delay time patterns from three 3D P and S wave models of the CSZ (Figure 5). Predictions made through the upper 50 km of the three models are compared to patterns in the observed average-station delay times, which should be most sensitive to near-surface features. Elevation and offshore sedimentation are not included and have been removed from the models. This has been done to isolate the impact of crustal and mantle velocities in the upper 50 km (impacts of sediments and elevation are presented in Section 5.2). Forward modeled delay times including sediments are presented in the supplement (Figure S5)

First, we evaluate P and S models from Gao (2018; G18; Figure 5a; Table 1), derived from full-waveform inversion of ambient noise. These models use both onshore and offshore data allowing them to span the entire region of interest. We restrict our use to the upper 50 km of the models. Delay time predictions are heterogeneous, with large variations over short wavelengths (<100 km) and peak delay times onshore that are more than double those of other models (evaluated below). Moreover, in several areas, such as beneath the coast and central Oregon, the P and S predictions deviate from one another. Neither the P nor S models result in a variance reduction of station-averaged delay times (Table 1).

Next are two hybrid models (Figures 5b and 5c) that consist of geographically limited offshore and onshore models which have been blended in order to span the region of interest. In both cases, the offshore P and

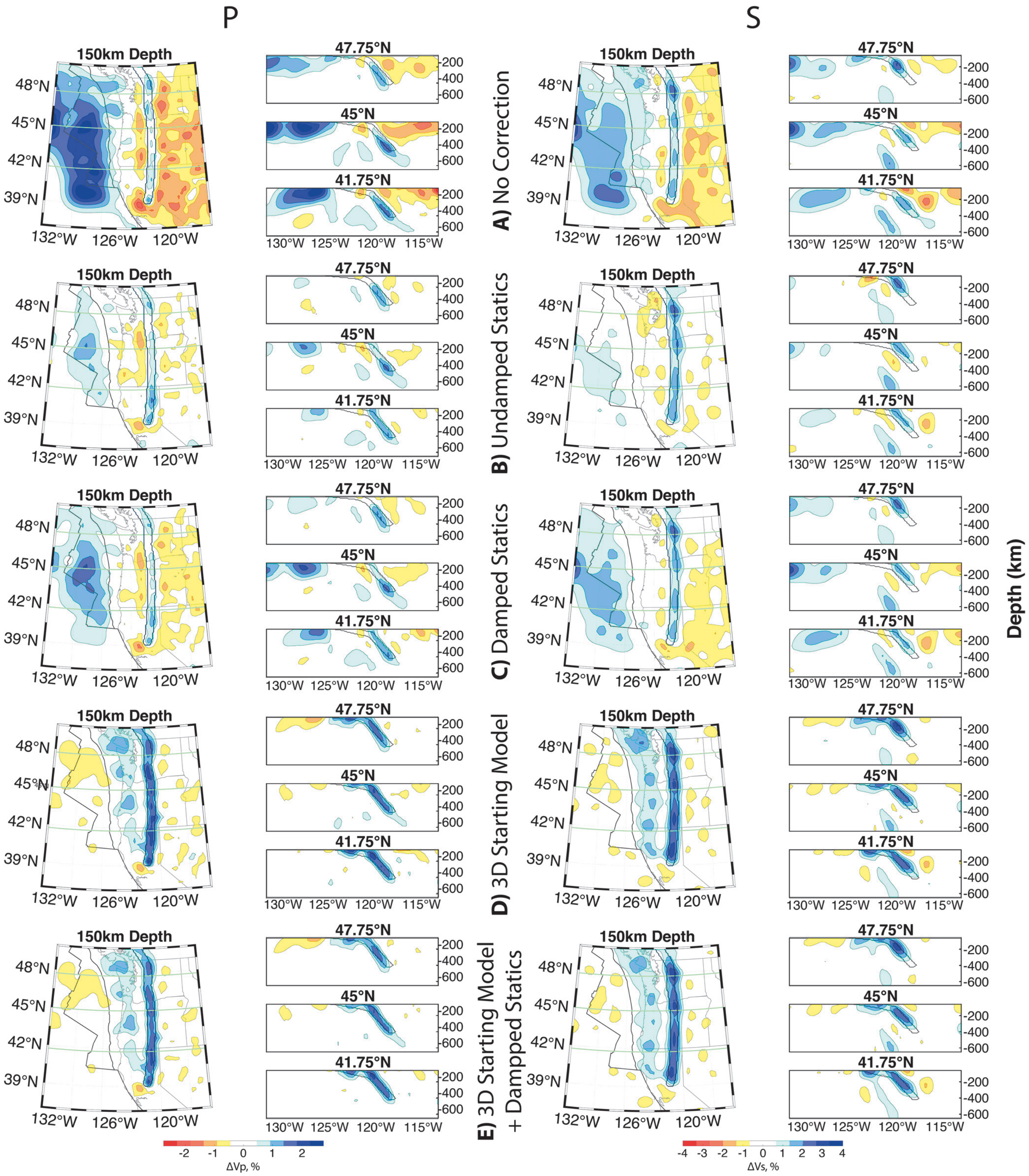

Figure 7. Inversion results for synthetic P and S datasets exploring different inversion strategies (see also Table 1). Synthetic delay times are calculated using the synthetic slab (Figure 6), the FakeCrust model in the upper 50 km, and elevation. Random perturbations to the model are used to simulate model uncertainty. (a) Panels show inversions where nothing has been done to account for near-surface structure. 1D flat-earth starting model. (b) Panels show inversions done with undamped station static terms. 1D flat-earth starting model. (c) Panels show inversions done with damped station statics. 1D flat-earth starting model. (d) Panels show inversions done using a 3D starting model (FakeCrust) of the upper 50 km and elevation. (e) Panels show inversions done using a 3D starting model, elevation, and heavily damped station statics. These statics have an RMS ~1/4 the size of those used in (b) Stations static values can be found in the supplement (Figure S12).

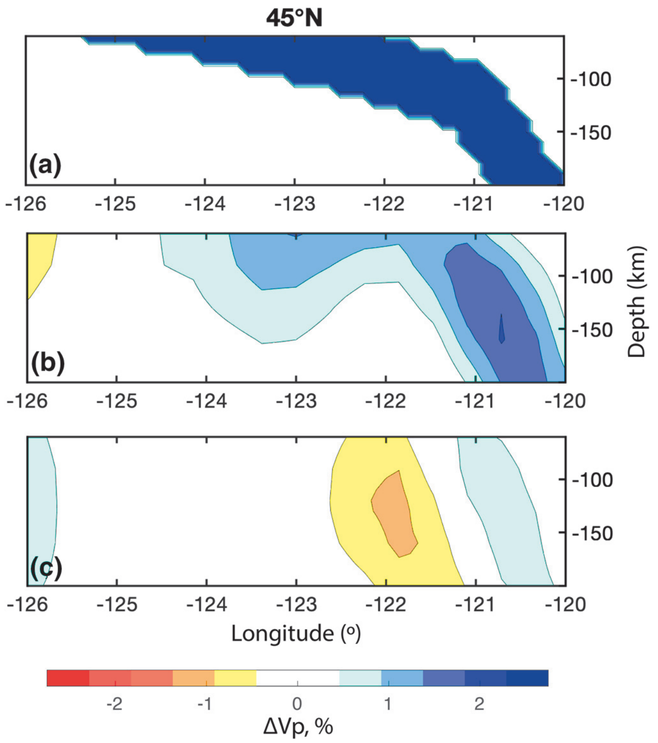

Figure 8. Comparison of inversion strategies on synthetic Vp data. (a) The synthetic input model zoomed in to the shallow dipping slab region and the underlying asthenosphere. (b) Synthetic inversion using a 3D starting model and heavily damped station statics (See Figure 6e). Slab structure is largely reconstructed; however, amplitudes are reduced and vertical streaking is present in the shallow dipping region. (c) Synthetic inversion using damped station statics (See Figure 6c). Slab structure is poorly reconstructed; low-velocity artifacts are present subslab and in the shallow dipping region.

S models come from Bell et al. (2016) [B16], produced using teleseismic Rayleigh wave data from the CI. Again, we restrict our use to the upper 50 km. Due to the low seismic frequencies used in this study, the upper 20 km is largely unconstrained by the surface wave data; however, this region is defined by a detailed starting model that includes an age-dependent lithosphere, variable thicknesses for oceanic crustal layers (2A, 2B, and 3), and a distinct forearc region. Though the focus of Bell et al. (2016) is S velocity structure, their model also includes P velocities, which largely reflect the starting model but are loosely constrained by the surface wave inversion (See Section 3.3 of Bell et al., 2016 for more details). To remove sharp discontinuities where the offshore model joins the onshore portion, they are smoothed together in a 100-km-wide band where they overlap offshore.

Figure 5b (Table 1) shows the delay time predictions from a model which combines B16 with onshore results from Delph et al. (2018) [D18]. D18 is an S wave model produced through joint inversion of Ps receiver functions and ambient noise cross-correlations measured largely using TA data. Here we use an extended version of the model with coverage out to −115°W. P-wave velocities were obtained from the S-wave model using the equations of Brocher (2005). Delay time estimates show clear onshore-offshore variation with the most delayed stations present in the forearc region. Two particularly delayed regions are present in the northern and southern forearc, due to pronounced low velocities in the model (Delph et al., 2018). This model is significantly less heterogeneous than G18.

Figure 5c (Table 1) shows the delay time predictions from a model which combines B16 with the onshore crustal model from Schmandt and Lin (2014) [SL14]. SL14 was developed specifically as a starting model for teleseismic body wave inversions (Schmandt & Lin, 2014). SL14 is a three-layer model (0–7 km, 7–15 km, and 15-Moho) with a variable crustal thickness spanning the continental United States. Crustal thicknesses do not exceed 50 km in our study region. Delay time estimates from this model are smoother than G18 and B16/D18 primarily due to the coarse parameterization. Clear onshore-offshore variations are present with the largest delays in the forearc similar to B16/D18, though the amplitude of the delays is reduced.

We find that the B16/SL14 model results in the largest reduction to the misfit of the observed station-averaged delay times in both the P and S datasets (Table 1). The B16/D18 model provides the second-largest reduction in misfit, with very similar reductions in P station-averages as B16/SL14. The G18 model increases the data misfit for both datasets but particularly for P, suggesting it is unreliable as an *a priori* constraint. During inversions of the observed data, we will use B16/SL14 as our preferred starting model (Section 6); inversions using alternative starting models can be found in the supplementary material (Figure S6).

5.4. Inverse Modeling of Synthetic Delay Times

To explore different inversion strategies, we generated a synthetic delay time dataset for a target 3D subduction zone velocity model and inverted these data under different assumptions. We evaluate these inversion strategies by their ability to reproduce the target model. This target model includes near-surface velocities from FakeCrust with added random heterogeneity and a high-velocity anomaly that mimics a subducting JdF slab (Figure 6).

Slowness perturbations representing the subducting JdF slab are defined by a 50-km thick, high-velocity anomaly ($\Delta Vp = 2\%$, $\Delta Vs = 4\%$) extending to 410 km depth (Figure 6). The slab is defined by shallow and steeply dipping sections. The upper interface of the shallow section follows the inferred slab depths of

McCrory et al. (2012) for depths of 50–100 km; below 100 km depth, the slab dip is 50°. Figure 6 (Table 1) shows inversions which contain only the synthetic slab, with no structure in the upper 50 km. This provides a benchmark for how well we can reproduce the mantle target in the absence of near-surface complexities given our data coverage. The dipping high-velocity slab is well recovered with few low-velocity anomaly artifacts in the surrounding region. The S inversions do image a secondary dipping high-velocity anomaly beneath the slab which is a known artifact. This artifact can be seen in all the S inversions and some of the P inversions described below and is likely a consequence of the dipping target structure and imperfect resolution of the dataset. This artifact is likely most pronounced in the S models because the S data is sparser, lower frequency, and larger variance than the P dataset.

The synthetic crustal structure is defined by an altered version of FakeCrust in the upper 50 km (Figure S3). Here, we apply random Gaussian perturbations with a standard deviation of ±4% to each node (10 km^3 region) of the FakeCrust model to simulate unknown local variations which will be unaccounted for by any of our applied starting models. Additional inversions with systematic variations can be found in the Supplement (Figures S7–S11). Gaussian noise ($\sigma = 0.25$ s) was added to the P and S synthetic delays to simulate uncertainty in the measurements and we use event-station distributions identical to those of the observed data. The model is sheared vertically to account for elevation. The initial RMS of the delay time residuals for the synthetic model are 0.40 s for P and 0.74 s for S.

We first invert the synthetic data for the model with a slab and 3D crustal structure, using only a flat (no elevation) 1D starting model (Figure 7a; Table 1). This is not a common methodology, as it assumes no near-surface variation, but it provides a worst-case scenario for identifying artifacts and resolution issues related to near-surface structure. The resulting images show large amplitude artifacts concentrated near the top of the model. The velocity anomalies vary laterally in a predictable manner (high-velocity offshore and low-velocity onshore), with a sharp gradient separating the regions. The anomalies are streaked vertically well below the 50-km limit of near-surface structure and they mask the slab anomaly, except in the deepest portions of the model.

Figure 7b (Table 1) shows the results of an inversion using a flat-earth, 1D starting model and undamped station static terms. Station statics are free parameters in the inversion that can absorb a delay time common to a station, an approach that is widely used (e.g., Dziewonski & Anderson, 1983; Hawley et al., 2016; Roth et al., 2008) due to ease of implementation. Our results show that station static terms absorb much of the near-surface structure, reducing anomalies at the top of the model. However, beneath the forearc in the upper 150 km, the inversion introduces margin-wide velocity reductions that we can identify as an imaging artifact. Consequently, high-velocities attributed to the shallow portion of the subducting slab (upper 100 km) are replaced with lower-velocity structures. We attribute this artifact to the heterogeneity of the forearc region, which includes the ocean-continent boundary, the shallow dipping portion of the slab, and the slab's transition to a steeper angle. While the synthetic slab anomaly is better imaged compared to Figure 7a, the upper 100 km of the slab is poorly recovered and down dip sections are lower in amplitude, which is likely due to station statics partially absorbing deeper structure. Station statics are presented in Figure S12.

We also investigate damped station statics where the magnitude of the statics are tuned to have a reduced influence (station static RMS is reduced by 25% and 45% for P and S respectively; Figures 7c and 8c; Table 1). Station statics are presented in Figure S12. There is a clear tradeoff between reducing artifacts due to onshore-offshore structure and the strength of the station static terms. Decreasing the magnitude of station statics leads to minor differences in anomalies beneath the forearc, but increases artifacts both offshore and onshore far from the margin nearly twofold. Most prominent in this model are high-velocity anomalies associated with the offshore structure in the upper 150 km. These anomalies are never fully removed, even in the undamped case, suggesting that at some point increasing the station static becomes less favorable than perturbing the model. Models with more realistic heterogeneity in the oceanic mantle may circumvent this issue as synthetic checkerboard tests with station statics do not show a similar feature. Low-velocity artifacts beneath the forearc are still present in the P model (Figure 8c) and the high-velocity shallow slab structure (50–100 km depth) is poorly reconstructed in both models.

Figure 7d (Table 1) shows the results of an inversion using a 3D starting model and no station statics. The starting model used is the unaltered FakeCrust model, sheared vertically to account for elevation. Note that the starting model is not identical to the model used to generate synthetic delays. This inversion is analogous to using an inferred velocity model to account for the near-surface structure under the assumption that it is correct to first-order but incorrectly estimates local variations. The inversion successfully reduces artifacts in the upper 150 km attributed to shallow structure, provides improved resolution of the subducting slab at all depths, and does not introduce low-velocity anomalies in the subslab region. Margin-wide high-velocity anomalies are observed beneath the forearc at 150 km depth connecting vertically to the region of the shallow dipping slab. We attribute this artifact to streaking due to near-vertical raypaths and note that this is a common problem in teleseismic body wave tomography. We suggest that a portion of the high-velocity anomaly due to the shallow slab (50–100 km depth) is being incorrectly mapped deeper into the model because of a lack of crossing rays. While this result better recovers the synthetic slab, the RMS is comparable to the undamped station static case, likely due to a change in the number of free parameters. Even though the RMS fits are similar, using the 3D starting model results in a structurally less-complex model—an important metric in addition to RMS by which to evaluate solutions and suggests that RMS misfit should not be the only metric by which a tomographic result is evaluated.

We also look at an inversion using the FakeCrust starting model (including elevation) and heavily damped station statics (Figures 7e and 8b; Table 1). Note, the damping used here is significantly more strict than that in Figure 7c (station static RMS is 68% and 75% less than the undamped case; 57% and 53% less than the damped case; P and S respectively). Station statics are presented in Figure S12. This approach represents a scenario where we use station statics primarily to account for structure not captured by our starting model, assumed to be local-scale perturbations. The results are similar to the starting model only case (Figure 7d), however, there is a reduction in low-velocity artifacts at the top of the model bringing it closer to the benchmark case. The shallow portion of the subducting slab is more accurately reconstructed (Figure 8b), though margin-wide high-velocity vertical streaking artifacts at ∼150 km remain.

While these inversions represent ideal conditions—synthetic data for a relatively simple, isotropic model—several general insights can be made. First, the station static terms absorb structure at many depths, not just near the surface. Because delay times are a path integrated measurement, as long as a majority of the incoming rays at a station sample a structure its contribution will be absorbed in the static; thus the station static cannot discriminate between a deep laterally expansive feature and a shallow constrained one. This can be observed in the synthetic results where structure below 50 km depth, particularly the laterally expansive slab, is being removed by the station statics. The inclusion of undamped station statics can introduce significant imaging artifacts, for example, in the subslab and shallow dipping slab regions near the ocean-continent transition. Second, using 3D starting models (including elevation) of shallow structure appears to better recover the slab particularly at depths <200 km, assuming that the model is correct to first-order. The models do result in significant high-velocity artifacts that are being streaked downward from the recovered slab in the forearc region. Lastly, we note that RMS misfit does not directly correspond to improved model reconstruction because station static terms absorb any contribution (not just shallow structure) that reduces the data misfit and increase the number of free parameters. Based on these results we conclude that the optimal inversion strategy is to use a detailed starting model, including elevation, and to use heavily damped station statics to account for local variations. These synthetic tests suggest that we should expect high-velocity artifacts in the forearc and use caution when interpreting such structures in that region.

6. Cascadia Subduction Zone Tomography

We present tomographic P- and S-wave results for the observed data, following the same inversion strategies described above (Section 6.1) and using our preferred inversion strategy (Section 6.2). By comparing tomographic inversions of the observed data using different strategies and considering our improved understanding from the synthetic results, we identify parts of the model influenced by our choice of inversion strategy and note potential artifacts.

For the synthetic studies (Section 5), we ignored the presence of offshore sedimentation, which is known to contribute to observed delay times (Section 5.2). Because sediment thicknesses are much less than our model grid spacing, we choose to adjust the delay times on a station specific basis according to the predictions

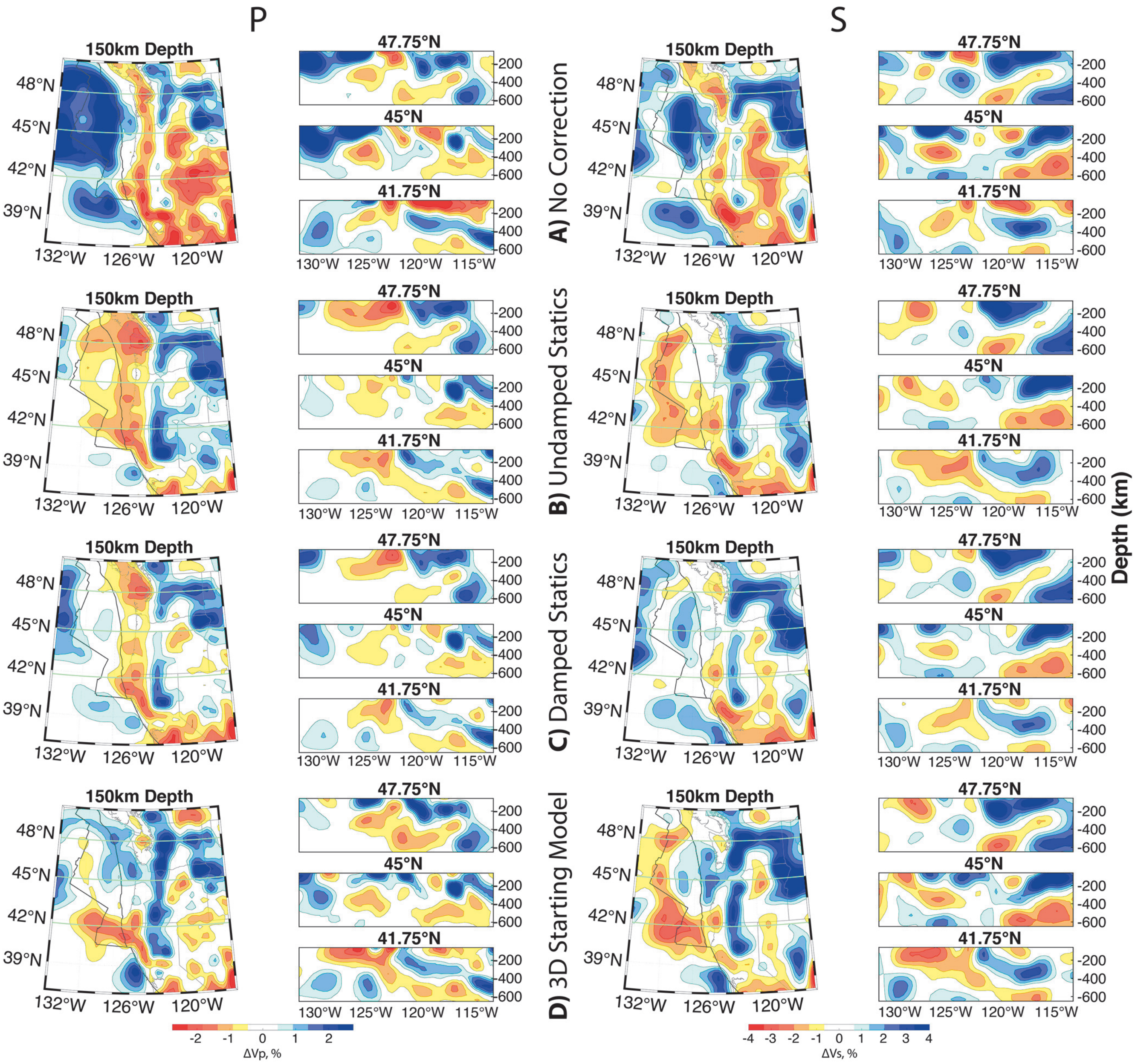

Figure 9. Inversion results of the observed P and S datasets exploring different inversion strategies (see also Table 1). Strategies used here are identical to those used in Figures 7a–7d. Site-specific corrections for offshore sedimentation have been performed prior to inversion. (a) Panels show inversions where nothing has been done to account for near-surface structure. 1D flat-earth starting model. (b) Panels show inversions done with undamped station static terms. 1D flat-earth starting model. (c) Panels show inversions done with damped station statics, tuned to reduce the onshore-offshore signal. 1D flat-earth starting model. (d) Panels show inversions done using a 3D starting model (B16/SL14; Section 5.3) of the upper 50 km and elevation. Stations static values can be found in the supplement (Figure S13).

shown in Figure 4b. Delay times are demeaned on a per-event basis after this correction; all the data in this section has been subject to this procedure.

6.1. Effect of Near-Surface Inversion Strategy

Figure 9a (Table 1) shows the results of inverting the observed delay time data using a 1D flat-earth starting model (e.g., Figure 7a). This inversion produces pronounced low- and high-velocity anomalies down to

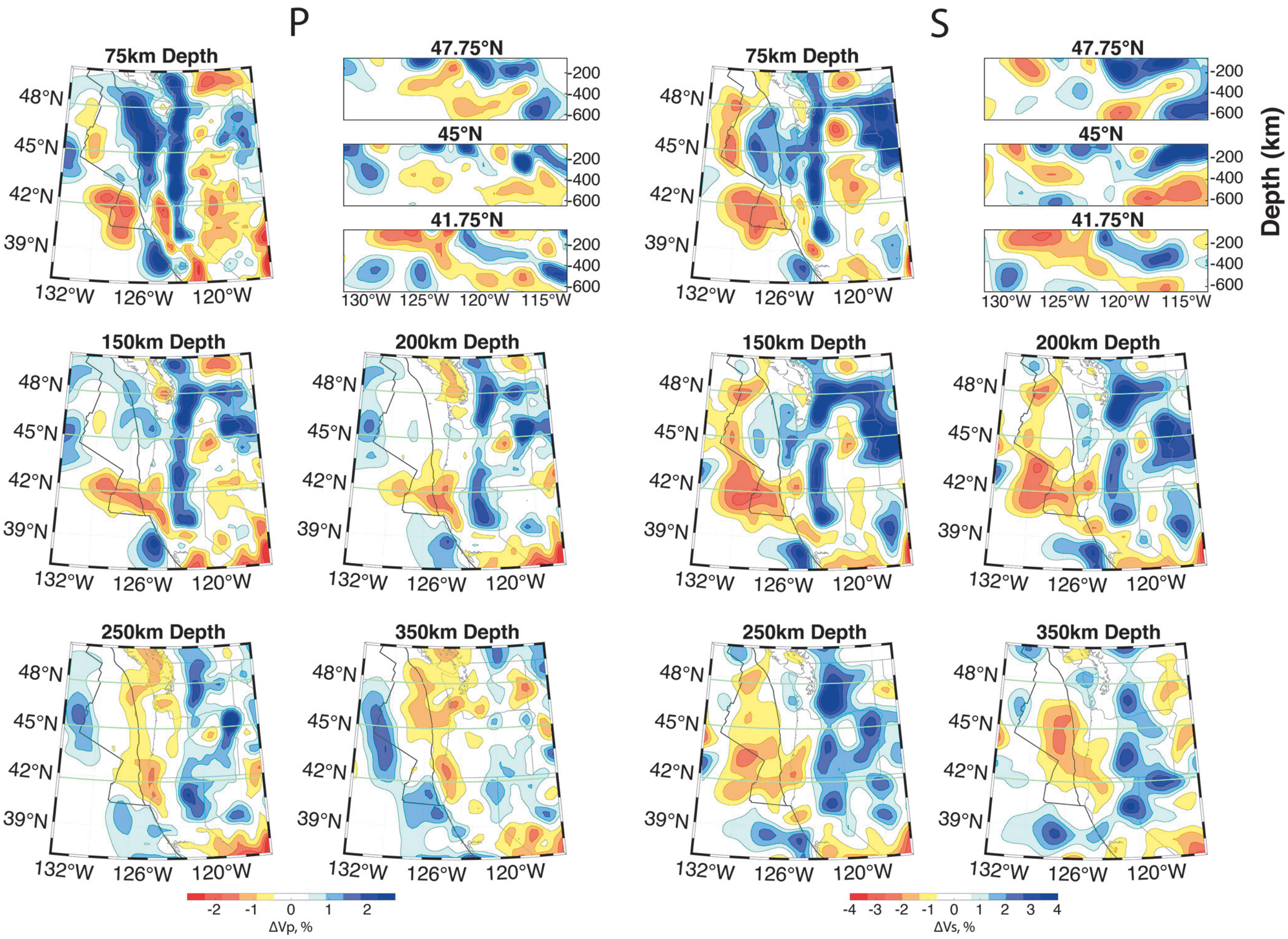

Figure 10. Inversion results from our preferred P and S tomographic models. The inversion strategy used to produce this model includes a 3D starting model (B16/SL14; Section 5.3) of the upper 50 km, known elevation, and heavily damped station statics. This inversion strategy is identical to that used in Figure 7e. The station static terms have an RMS ~1/5 of those used from the undamped case in Figure 9b. Stations static values can be found in the supplement (Figure S13).

200 km depth beneath the continental and oceanic regions, respectively. Beneath much of the JdF plate, high-velocity anomalies are attributed to unaddressed variations in elevation and crustal thickness. Beneath the western United States, high-velocity anomalies are present in a north-south trend near the volcanic arc and broadly beneath western Idaho. Pronounced low-velocity anomalies are recovered at asthenospheric depths throughout much of the continent. Cross-sections show dipping high-velocity perturbations consistent with a subducting slab, imaged at depths below 150 km but obscured at shallower depths where large low-velocity anomalies are present. A band of low-velocity anomalies is present beneath the forearc at 50–200 km depth. Synthetic results indicate that many of the structures in the upper 200 km are likely artifacts due to vertically smeared shallow structure and delay time errors due to the flat-earth assumption. High-velocity anomalies near the bottom of the model (500–600 km), particularly in the S images, may be artifacts due to imperfect resolution of the dipping high-velocity anomaly structure of the subduction zone like those seen in Figure 6a.

Figure 9b (Table 1) shows tomographic results assuming a 1D, flat-earth starting model and using undamped station static terms (e.g., Figure 7b). This workflow reduces the onshore-offshore variation reconstructed in the previous inversion. The RMS of the station static terms is similar to the starting RMS of the entire dataset (Table 1; Figure S13). Broad low-velocity anomalies are present offshore in the upper 200 km beneath the entirety of the oceanic plate, with a concentrated high amplitude band in the subslab region at 100–200 km depth. Onshore, low-velocity anomalies in the upper 200 km are reduced in most regions and high-velocity anomalies associated with the slab increase in amplitude. The slab is imaged well at depths below 150 km, however, at shallower depths, there is little evidence of a shallow dipping slab, with low-velocity anomalies throughout most of the forearc. Our synthetic studies indicate that low-velocity, subslab anomalies, and poor amplitude recovery of the shallow slab are artifacts of a workflow that only uses station statics to account for elevation and near-surface structure.

We also look at the effect of damped station statics in Figure 9c (Table 1; Figure S13). Here we see a reduction in the onshore-offshore variation in the upper 150 km, however, this requires a rather loose damping constraint. A band of low-velocity anomalies is present beneath the forearc and there is no evidence for a shallow dipping section of the slab. The presence of these anomalies, even in the damped case, along with our synthetic tests (e.g., Figure 7b) indicates that margin wide low-velocity anomalies are an artifact of using station statics.

Inversion results using a 3D starting model of the upper 50 km, known elevation, and no station statics are shown in Figure 9d (Table 1). We choose to use the B16/SL14 model as it provides the largest improvement in the average-station delay times (Section 5.3). We observe heterogeneous offshore structure, high-velocity anomalies beneath the central Cascadia forearc at ∼150 km, and an absence of margin wide low-velocity anomalies beneath the slab (∼150 km depth). Observations of low-velocity anomalies beneath the JdF ridge and the GDZ are broadly consistent with recent tomographic studies of offshore structure (Bell et al., 2016; Byrnes et al., 2017), though in detail they vary because our starting model already contains much of the offshore heterogeneity (see Supplement for details). High-velocity anomalies beneath the central forearc are consistent with a vertically streaked artifacts observed in our synthetics (Figure 7d and 8b) and suggest an incorrect mapping of shallow slab structure (50–100 km depth) deeper into the model. The absence of broad low-velocity anomalies in the upper 150 km of the forearc (replaced by localized subslab anomalies north and south) and the presence of a high-velocity artifacts only beneath the central Cascadia forearc, along with our synthetic tests suggest that the subslab mantle is heterogeneous along strike.

6.2. Preferred Tomographic Model

Our preferred tomographic models are presented in Figure 10 (Table 1). These inversions use the B16/SL14 3D starting model (see Figure S6 for alternative models), known elevation, and heavily damped station statics (station static RMS 81% and 88% less than the undamped case; 77% and 78% less than the damped case; P and S respectively). The size of our station statics (Figure S13) is consistent with the local variation observed in 2D refraction profiles (Section 5.1) and can be seen to have a subtle but beneficial influence in our synthetic tests (Section 5.4).

The models display significant heterogeneity in both onshore and offshore regions, especially in the upper 200 km. Peak-to-peak variations in velocity structure are on the order of 7% for P and 10% for S, with the largest contrast between the offshore Gorda structure (upper 200 km) and the subducting slab (75–350 km). The range of variation is comparable to that observed in Schmandt and Humphreys (2010a) (7.8% and 14.5%, P and S respectively). Offshore variations arise primarily from low-velocity anomalies beneath Gorda, the JdF Ridge, and northwest Washington, juxtaposed with high-velocity anomalies in the JdF plate interior (75 km depth).

The N-S trending, dipping high-velocity anomaly structure we image at ∼121°W is consistent with the subducting JdF slab inferred by previous studies (e.g., Obrebski et al., 2010; Roth et al., 2008; Schmandt and Humphreys, 2010; Tian and Zhao, 2012). We image several common features of the slab in both P and S such as along strike variability, and a maximum penetration depth near the transition zone. In the southern section of the subduction zone, large-amplitude high-velocity anomalies persist down to at least 350 km depth and are the most compact slab features along strike. The northern section is also imaged to at least 350 km while, in the central portion, the amplitude of slab anomalies decreases at depths below 200 km in the P model becoming faint to nonexistent in places (referred to as the slab "hole" Obrebski et al., 2010; Roth et al., 2008; Tian and Zhao, 2012). However, this is less pronounced in the S model where high velocities are reconstructed at depths of 350 km in central Cascadia. We image positive anomalies for both P and S in the central portions of the slab at depths above 150 km, which connect to high-velocity anomalies associated with the JdF plate. These anomalies are consistent with vertical streaking of a shallow dipping slab (50–100 km depth).

Other onshore features of the P and S models include high-velocity anomalies throughout eastern Washington/Oregon and into Idaho (75–200 km) consistent with an ancient Farallon slab curtain (Schmandt & Humphreys, 2011) and small-scale, high-velocity anomalies (200–250 km) beneath the Wallowa mountains (Darold & Humphreys, 2013; Stanciu & Humphreys, 2020). We also image large-amplitude, east-dipping high-velocity anomalies at transition zone depths consistent with the fragmentation of old Farallon slab (James et al., 2011; Schmandt and Humphreys, 2010). We note that several of these anomalies are located near the eastern edge of our model and may be less well-resolved given the station distribution.

Offshore, we image low-velocity anomalies in the upper 150 km of both P and S models beneath the JdF Ridge region and the GDZ. This indicates that there is significant structure below 50 km depth as our 3D starting model already contains heterogeneity in the upper 50 km. Anomalies associated with the spreading center have an asymmetric structure that changes along axis. North of Axial Seamount low-velocity anomalies are present west of the ridge, transitioning east of the ridge to the south near the Blanco (upper 100 km). Beneath the GDZ a broad low-velocity anomaly exists that is poorly correlated with nearby tectonic boundaries or plate age. East of the JdF Ridge we image high-velocity anomalies beneath the older sections of the plate (75 km depth) with the largest anomalies occurring in the northern section near the trench for P and the center of the plate for S. High-velocity anomalies in the upper 150 km just east of the deformation front are consistent with the vertical streaking seen in our synthetic inversions (Section 5.4).

Beneath the subducting slab of both P and S models, we image two regions of lower velocities in the northern and southern parts of the subduction zone (100–250 km; 41.75°N and 47.75°N). The northern anomaly lies beneath the Olympic mountains near where the slab strike changes to be more westerly and the subduction angle shallows (McCrory et al., 2012). The anomaly center is approximately 200 km south of the northern slab edge (Audet et al., 2008) and because of station coverage, it is unclear how far north it extends. This anomaly is much more pronounced in the P-wave model. The southern anomaly lies at the very edge of the slab (Beaudoin et al., 1998) and appears to connect at shallower depths to low-velocity anomalies directly beneath the Gorda. Subslab low-velocity anomalies are localized and do not connect as a coherent margin-wide, subslab feature (see 45°N).

7. Discussion

Our analyses provide several key insights into how methodological choices influence inversion results and the degree of confidence we have in specific features of the CSZ. In Section 7.1, we discuss the important role that inversion strategy has in the imaging and interpretation of shore-crossing datasets, as well as the pitfalls of those methods. We then discuss the subslab asthenosphere, where inversion strategy impacts the recovered anomalies, leading to differing interpretations of regional mantle dynamics (Section 7.2). We then compare the preferred models to our previous images of the CSZ (Section 7.3). In Section 7.4, we discuss the similarities and differences between P and S models and their implications. Finally, in Section 7.5 we discuss the limitations of our models.

7.1. Importance of Onshore-Offshore Starting Models

Crustal thickness, elevation, and sediment thickness variations between the onshore-offshore regions lead to significant signal in P- and S-wave delay time data, which left unaccounted for, dominate the upper 200 km of tomographic images and obscure mantle structures at all depths. We focus on the CSZ, but our findings are applicable to any region containing oceanic-continental plate boundaries or large crustal heterogeneities (Waldhauser et al., 2002). Further, we argue that even without detailed onshore-offshore velocity models, one can still build a useful 3D starting model from elevation, crustal thickness, and sediment thickness information, which is available in coarse resolution globally. Such a model will reduce first-order imaging artifacts without relying on inversion parameters like station statics but instead utilizing independently derived structural constraints.

Both synthetic and observed tomographic models show that the choice of inversion strategy influences the resulting image and thus directly impacts how we interpret key features. Our synthetic tests suggest that these variations occur most predominately where shallow structure changes rapidly and/or has a complex relationship with deeper structures, which is the case beneath the CSZ forearc (Figure 8). We suggest that careful consideration of inversion strategy is necessary to avoid overinterpretation of potential imaging artifacts.

We prefer a strategy that accounts for near-surface variations by using a 3D starting model that is derived from independent seismic constraints, explicitly includes elevation, incorporates station-specific corrections for sediment delays, and includes heavily damped station statics to account for local structure. In this approach, the first-order effects on a delay time (elevation and crustal thickness) are accounted for by our starting model. Sediments, which are site-specific, are handled as an *a priori* adjustment to the delays. This leaves only structure that we have no reasonable way to constrain (site effects, small scale heterogeneity, and timing offsets) to be handled by station statics. We find that station statics are still useful to account for unknown structure but believe they should be recalibrated as more independent constraints become available with the goal of reducing them as much as possible.

We caution against using station static terms alone, particularly in a subduction setting, as they can lead to unwanted artifacts and underrecovered structure in the upper 200 km (Figure 8). Station static terms depend on the integrated time along ray paths and are only constrained by how well they reduce the overall data misfit, thus they tend to absorb and are sensitive to deeper mantle structures (Robertson & Woodhouse, 1997). This becomes problematic when imaging structures with a broad lateral extent such as a shallowly dipping slab with subvertical rays, because most of the incoming ray paths will sample the structure regardless of depth, making it favorable to absorb the signal contribution. Further, because the amplitude of the station static term depends on the demeaned delay time dataset, the array geometry, data distribution, and measurement errors can influence the estimated correction in a manner that is not easy to predict.

We note that our preferred methodology is not without its own shortcomings. First, even with a detailed starting model, certain regions such as the forearc are difficult to constrain and are likely sources of error due to incorrect modeling. Our dataset does not appear to be particularly sensitive to systematic errors in this region (Figures S7–S11) but this may not be the case elsewhere. Second, our methodology introduces margin-wide high velocity artifacts in the forearc at ~150 km depth. These artifacts are likely due to vertical streaking as shallow slab structure is incorrectly mapped to deeper portions of the model. We find this type of artifact preferable to the low-velocity artifacts introduced by station statics because their origin is clearer and they are directly related to an expected structure (i.e., the shallow slab).

7.2. Improved Resolution Beneath the Forearc and Identification of Artifacts

The region most influenced by our joint onshore-offshore dataset is the forearc, specifically in the subslab asthenosphere where onshore and offshore event-station pairs share ray paths. The oceanic asthenosphere is of particular interest because it is the region separating and governing the interaction between the lithosphere and the deeper convecting mantle. The oceanic asthenosphere's relationship to lateral tectonic plate motions and broader density/pressure conditions is not straightforward (Bodmer et al., 2015; Lin et al., 2016) and is further complicated in subduction systems where the vertical motion of the slab influences the asthenospheric response. It is unclear what role the oceanic asthenosphere plays in decoupling the plates from the mantle, in magma generation, and as source material for nearby volcanic systems, and in transporting anomalous material, such as from nearby hotspots. Moreover, there is still debate concerning the nature of seismic anomalies observed in the subslab asthenosphere and what impact they have on subduction dynamics (Bodmer et al, 2018, 2020; Hawley et al., 2016; Portner et al., 2017).

We image two prominent localized subslab, low-velocity features in the northern and southern sections of the CSZ between 100 and 250 km depth in P and 60–200 km depth in S. Low-velocity anomalies are not present in central Cascadia, where we find high-velocity anomalies interpreted as streaking artifacts. Our synthetic tests suggest that downward streaking of the shallow slab due to our methodology occurs margin-wide. Thus, we expect to find high-velocity anomalies at 150 km depth beneath the entire forearc. Because we image the opposite in the north and south (lower velocities subslab) we conclude that the subslab mantle is heterogeneous. We caution that because artifacts are still likely in this region it is difficult to directly interpret amplitudes, however, the relative patterns of heterogeneity of subslab mantle appear to be robust.

Localized low-velocity anomalies have previously been interpreted to be regions of mantle upwelling (Bodmer et al., 2018; Chen et al., 2015). Bodmer et al. (2018) inferred that these anomalies are regions of partial melt (due to decompression melting), associated with entrainment of nearby hotspot material into the subduction zone and plate fragmentation processes in the GDZ, for the northern and southern anomalies respectively. The inferred buoyant nature of the anomalies could impact the behavioral segmentation of the CSZ megathrust and forearc by modulating the total resistive shear force on the megathrust interface (Bodmer et al, 2018, 2020).

This result contrasts with the recent onshore-offshore P-wave tomography of Hawley et al. (2016), which images subslab low-velocity anomalies (~150 km depth) along the entire subduction zone. These anomalies are interpreted as an accumulation of buoyant asthenosphere subslab, originating from a thin weak layer separating the oceanic lithosphere and underlying mantle. We suggest that the discrepancy between our results and those of Hawley et al. (2016) arises from differences in the inversion strategies, specifically the use of station statics to account for shallow structure. We infer that our inversion of the observed data using damped station statics (Figure 9c) is analogous to the Hawley approach and similarly recovers broad margin-wide low-velocity anomalies subslab. However, our synthetic tests show that margin-wide anomalies are an imaging artifact of this workflow.

7.3. Update of Previous Tomographic Models

The preferred tomographic models presented here (Figure 10) represent a significant update to our previous work in the region (Bodmer et al., 2018; Byrnes et al., 2017). Our S model utilizes an expansion of the delay time dataset used in Byrnes et al. (2017) to include onshore stations and a 3D starting model for structure in the upper 50 km; Byrnes et al. (2017) used a 1D starting model. Our P model uses the same delay time dataset as Bodmer et al. (2018) but uses an updated starting model, sediment thickness map, and inversion parameters. Details of changes between models are presented in the Supplementary text.

Our P wave model is generally consistent with Bodmer et al. (2018), however, there are regions of significant difference, particularly offshore and beneath the forearc. Low-velocity anomalies in the north and south interpreted to be localized upwellings in Bodmer et al. (2018) are still present but differ in amplitude. Most notably the northern anomaly is decreased by ~1.5%. This does not contradict the interpretations that subslab buoyancy influences megathrust segmentation (Bodmer et al., 2018, 2020), as the spatial correlations highlighted remain and the velocity anomalies in the north and south are significant (Figure S14). It does suggest that buoyancy estimates in the north were overpredicted, with revised calculations reducing the predicted buoyancy anomaly in the north by ~1/2, values closer in amplitude with those in the south.

Offshore, our updated P model has more distinct low-velocity anomalies beneath the JdF Ridge at depths above 100 km, a feature more consistent with S-wave models (Bell et al., 2016; Byrnes et al., 2017). Below 150 km the updated model appears to be generally faster, with high-velocity anomalies more present in the central Cascadia forearc, less pronounced plate-wide low-velocities at depths below 300 km, and greater connectivity of the slab structure. We still observe low-velocity anomalies connecting the northern subslab anomaly back to the JdF Ridge consistent with a hotspot origin, but they are reduced in amplitude.

Our S model is broadly consistent with Byrnes et al. (2017), with the largest differences occurring beneath the forearc. Byrnes et al. (2017) imaged pronounced high-velocity anomalies that extended east to the margin, but our updated model shows significantly more heterogeneity beneath the forearc. This is likely due to the previous model only using offshore data west of the margin shelf. Beneath the JdF plate we image reduced high-velocity anomaly amplitudes (~1.5% lower), with a similar reduction in low-velocity amplitudes beneath the ridges. Low-velocity anomalies in the upper 100 km are asymmetric about the JdF Ridge, sharply grading into high-velocity anomalies beneath the plate, consistent with the interpretation of dynamic upwelling and subsequent downwelling, though the strength of the asymmetry is less pronounced. At depths below 150 km, asymmetry associated with the ridge disappears as low-velocity anomalies merge into a plate-wide anomaly below 300 km depth. Differences such as amplitude reduction and less pronounced ridge asymmetry are not unexpected as our starting model contains structure from Bell et al. (2016) in the upper 50 km. Thus, much of the heterogeneity has already been accounted for, especially for melting-related processes that are significant in the 30–50 km depth range.

7.4. Comparison of P- and S-wave Structure

To first-order, our P and S models are consistent, a condition that is not guaranteed since the datasets are inverted independently. While a direct comparison of P and S anomaly amplitudes cannot be done in this work due to the relative, demeaned nature of the data, future joint inversions of the P and S body wave data would likely provide additional structural constraints and will be presented elsewhere. Broad comparison of the P and S models can identify common features, these include recovery of the subducting slab down to ∼350 km, the Idaho curtain high-velocity anomalies, reduced velocities in the northern and southern subslab region, lower velocities beneath the Gorda region, and lower velocities beneath the JdF Ridge.

The consistency between models suggests that these features reflect true first-order structures, however, as the P and S data have different sensitivities and resolution, we caution against overinterpretation. For example, our P and S datasets differ in their frequency content and size, with the S delays being less abundant and measured at longer periods, leading to a smoother less finely resolved model. Additionally, P and S waves have different sensitivities to properties such as partial melt and seismic anisotropy (Hammond & Toomey, 2003), both of which have been inferred to be important in this region. Lastly, we reiterate that because the measurements are relative and the models are not coupled, anomalies likely do not reflect variation around a common reference.

There are significant differences between the models, which may suggest compositional variations and/or anisotropic heterogeneity. High-velocity anomalies associated with the slab become segmented at depths below ∼200 km in both models, however, the spatial distribution is not consistent. In the P-wave model two higher-velocity sections are observed in the north and south (below 200 km), while the central section (∼43–45.5°N) is reduced in amplitude. The S-wave model instead appears to be segmented into three higher-velocity sections separated by shorter sections of reduced amplitude (44.5–45.5°N and 41–42°N). Segmentation of slab high-velocity anomalies at depth appears to be a robust feature but it is unclear what the exact spatial extent is, an important distinction to understanding if this is a tear, a large gap, or an imaging artifact. The most robust reduction in both models at 45°N places a segment boundary further to the north than suggested by recent S-wave imaging (Hawley & Allen, 2019).

The nature of slab fragmentation in the upper mantle should influence slab rollback, mantle flow, and tectonic stresses in the region. The P model, with a ∼200-km-wide velocity reduction in central Cascadia, is consistent with a larger feature such as a slab hole or a widening slab tear. However, the P velocity reduction is not as pronounced as in previous models and the S model suggests compact velocity reductions and high-velocity anomalies in central Cascadia, consistent with a more connected slab at depth. Our choice of inversion strategy appears to have an influence on this as models using station statics are less connected at depth than those using a 3D starting model. We do note, however, that the S model has lower resolution and that direct comparison of the P and S slab geometry is difficult because the models are uncoupled. Further, seismic anisotropy could have a large impact on how the slab is resolved, with synthetic tests suggesting that unaccounted for anisotropy can mask the true slab geometry (Bezada et al., 2016; VanderBeek & Faccenda, 2020). Because teleseismic P and S waves have different sensitivities to anisotropy, particularly if it is dipping, this may account for the discrepancy between the models.

In the subslab, low-velocity anomalies imaged in the north and south vary both in amplitude and location in the P and S models. Low-velocity anomalies in the S-wave model are imaged closer to the surface (by ∼50 km, notably in the north). This likely is impacted by our choice of starting model, as our synthetic tests show that reconstructed velocity anomalies in the upper 100 km are affected by model choice and that erroneous near-surface structure can move mantle anomalies vertically. If subslab low-velocities are regions where partial melt is present, we may expect local increases in Vp/Vs (Hammond & Humphreys, 2000). In the western United States, where partial melt has been inferred at similar depths, Vp/Vs perturbations of up to 7% have been observed (Schmandt & Humphreys, 2010a). However, the northern subslab low-velocity anomaly appears less pronounced in the S-wave model than in the P-wave model. Additionally, this anomaly appears to connect back to the JdF Ridge in the P-wave model while in the S-wave model this connection is not apparent or occurs significantly to the north.

In the upper 150 km beneath the ridge, low-velocity anomalies in S appear to be larger amplitude than their P counterparts, possibly suggesting increased Vp/Vs and melt content at depths below the hydrous melting regime. Anomalies in both models also appear to be asymmetric about the ridge, which has been observed in S previously offshore (Bell et al., 2016; Byrnes et al., 2017), consistent with dynamic upwelling and off-axis downwelling. Further constraints on Vp/Vs here may help to define the percentage of partial melt present (Eilon & Abers, 2017).

7.5. Limitations

We suggest that our 3D starting model (B14/SL14; Section 5.3) approximates the first-order CSZ near-surface structure and consequently improves the reliability of our tomographic images; however, improvements to the starting model and its implementation in the forward problem can and should be made in future studies. Notably, structure in the forearc has been shown to be particularly anomalous and can negatively impact surface wave inversions due to sharp changes in sensitivity (Janiszewski et al., 2019). Our starting model is an amalgamation of available onshore and offshore surface wave models, which likely leads to errors where the models overlap. Additionally, because the shelf and coastline represent the edges of the respective models, this is a region where they lose resolution. We tested the sensitivity of this region to erroneous structure by inserting 6% perturbations to the forearc (0–50 km depth), values consistent with the standard deviation of global compilations (Figures S7–S9). Back of the envelope calculations estimate a 6% perturbation to result in a ~0.5 s change in delay time, a ~14 km variation in crustal thickness, ~4 km change in elevation, or ~1 km of offshore sedimentation. We find that our preferred methodology is relatively insensitive to systematic perturbations in the forearc and erroneous structure here is not mapped deeper into the model.

As more onshore-offshore results from teleseismic surface waves, ambient noise, and receiver functions become available, starting models can be further refined and compared. Similarly, joint inversion of body and surface waves could further constrain the near-surface structure, improving the reliability of body waves, while further constraining key depths where the data sensitivities overlap. As models improve, the reliance on station statics should be reduced, with station statics still playing a role but requiring user defined damping to trade off with known structures.

Further, the assumption that the CSZ velocity structure is isotropic is almost certainly violated. Onshore and offshore studies suggest that strong anisotropy exists at mantle depths throughout the region of interest (Bodmer et al., 2015; Eilon & Forsyth, 2020; Martin-Short et al., 2015; VanderBeek & Toomey, 2017, 2019). Compounding this, these studies suggest that the patterns of anisotropy are heterogeneous, and considering the nearby dipping slab, likely have a significant radial component. Though many features of our isotropic model appear robust, we caution that until the effects of CSZ anisotropy are better characterized and incorporated into the tomographic inversion, uncertainty remains (Bezada et al., 2016).

8. Conclusions

We present onshore-offshore tomography of the CSZ for which we have conducted a series of synthetic and observed data inversions for P- and S-wave velocity models. We conduct several tests, exploring different inversion strategies and starting models, aimed at reducing contamination from unaccounted for structure in the upper 50 km. These tests provide a way to evaluate: (1) What the largest contributors to onshore-offshore variation are, (2) the effect that globally available datasets have on measured delay times, (3) the effect of multiple starting velocity models on delay times and tomographic results, leading to the choice of a preferred starting model, and (4) the effect of multiple inversion strategies, leading to the choice of a preferred methodology.

The largest near-surface contributions to delay time variations come from crustal thickness and elevation (in roughly equal amounts), followed by offshore sediments (particularly for S). Synthetic tests show that using station statics alone to account for this structure leads to imaging artifacts, particularly below the forearc, and reduction of velocity amplitudes for known structures. We prefer an inversion strategy that uses a detailed 3D starting model, including elevation, and heavily damped station statics to account for local variations.

We perform the same suite of inversion strategies used in the synthetic analysis on the observed data, allowing us to identify potential artifacts and better understand their origin. We conclude that margin wide low-velocity anomalies beneath the forearc are an artifact resulting from station statics. Our preferred P-and S-wave models appear to be consistent to first-order, imaging low-velocity anomalies in the northern and southern subslab region, near the JdF Ridge, and beneath the GDZ. Variations in P and S low-velocity anomalies may reflect Vp/Vs structure and the presence of partial melt; future joint inversions will allow robust interpretation of Vp/Vs structure. High-velocity anomalies associated with the subducting slab are observed in both models but differences at depths below 200 km in central Cascadia call into question the nature of the slab hole.

Data Availability Statement

Seismic data used in this research were provided by instruments from the Ocean Bottom Seismic Instrument Center (https://obsic.whoi.edu/), funded by the National Science Foundation. OBSIC data are archived at the IRIS Data Management Center (http://www.iris.edu). This work benefited from access to the University of Oregon's high-performance computer, Talapas (https://hpcf.uoregon.edu/content/talapas).

Acknowledgments
We thank Brandon Schmandt for sharing his P and S delay time dataset for the western United States. We thank Sam Bell, Donald Forsyth, Haiying Gao, and Jonathan Delph for sharing their surface wave models with us. We thank William Hawley and an anonymous reviewer for their insightful comments that helped improved the manuscript. This work was funded by the National Science Foundation under grants OCE-1948961 and OCE-1520694 to the University of Oregon.

References

Atwater, T. (1970). Implications of Plate Tectonics for the Cenozoic Tectonic Evolution of Western North America. *Geological Society of America Bulletin*, *81*(12), 3513. https://doi.org/10.1130/0016-7606(1970)81[3513:ioptft]2.0.co;2

Atwater, T., & Stock, J. (1998). Pacific-North America Plate Tectonics of the Neogene Southwestern United States: An Update. *International Geology Review*, *40*(5), 375–402. https://doi.org/10.1080/00206819809465216

Audet, P., Bostock, M. G., Christensen, N. I., & Peacock, S. M. (2009). Seismic evidence for overpressured subducted oceanic crust and megathrust fault sealing. *Nature*, *457*(7225), 76–78. https://doi.org/10.1038/nature07650

Audet, P., Bostock, M. G., Mercier, J. P., & Cassidy, J. F. (2008). Morphology of the Explorer/Juan de Fuca slab edge in northern Cascadia: Imaging plate capture at a ridge-trench-transform triple junction. *Geology*, *36*, 895–898. https://doi.org/10.1130/G25356

Beaudoin, B. C., Hole, J. A., Klemperer, S. L., & Tréhu, A. M. (1998). Location of the southern edge of the Gorda slab and evidence for an adjacent asthenospheric window: Results from seismic profiling and gravity. *Journal of Geophysical Research*, *103*(B12), 30101–30115. https://doi.org/10.1029/98jb02231

Becker, T. W. (2012). On recent seismic tomography for the western United States. *Geochemistry, Geophysics, Geosystems*, *13*(1), 1–11. https://doi.org/10.1029/2011GC003977

Bell, S. W., Ruan, Y., & Forsyth, D. W. (2015). Shear velocity structure of Abyssal plain sediments in Cascadia. *Seismological Research Letters*, *86*(5), 1247–1252. https://doi.org/10.1785/0220150101

Bell, S., Ruan, Y., & Forsyth, D. W. (2016). Ridge asymmetry and deep aqueous alteration at the trench observed from Rayleigh wave tomography of the Juan de Fuca plate. *Journal of Geophysical Research: Solid Earth*, *121*(10), 7298–7321. https://doi.org/10.1002/2016JB012990

Bezada, M. J., Faccenda, M., & Toomey, D. R. (2016). Representing anisotropic subduction zones with isotropic velocity models: A characterization of the problem and some steps on a possible path forward. *Geochemistry, Geophysics, Geosystems*, *17*(8), 3164–3189. https://doi.org/10.1002/2016GC006507

Bezada, M. J., Humphreys, E. D., Toomey, D. R., Harnafi, M., Dávila, J. M., & Gallart, J. (2013). Evidence for slab rollback in westernmost Mediterranean from improved upper mantle imaging. *Earth and Planetary Science Letters*, *368*, 51–60. https://doi.org/10.1016/j.epsl.2013.02.024

Bodmer, M., Toomey, D. R., Hooft, E. E. E., Nábelek, J., & Braunmiller, J. (2015). Seismic anisotropy beneath the Juan de Fuca plate system: Evidence for heterogeneous mantle flow. *Geology*, *43*(12), 1095–1098. https://doi.org/10.1130/G37181.1

Bodmer, M., Toomey, D. R., Hooft, E. E. E., & Schmandt, B. (2018). Buoyant asthenosphere beneath Cascadia influences megathrust segmentation. *Geophysical Research Letters*, *45*(14), 6954–6962. https://doi.org/10.1029/2018GL078700

Bodmer, M., Toomey, D. R., Roering, J. J., & Karlstrom, L. (2020). Asthenospheric buoyancy and the origin of high-relief topography along the Cascadia forearc. *Earth and Planetary Science Letters*, *531*, 115965. https://doi.org/10.1016/j.epsl.2019.115965

Brocher, T. M. (2005). Empirical relations between elastic wavespeeds and density in the Earth's crust. *Bulletin of the Seismological Society of America*, *95*(6), 2081–2092. https://doi.org/10.1785/0120050077

Brudzinski, M. R., & Allen, R. M. (2007). Segmentation in episodic tremor and slip all along Cascadia. *Geology*, *35*(10), 907. https://doi.org/10.1130/G23740A.1

Burgette, R. J., Weldon, R. J., & Schmidt, D. A. (2009). Interseismic uplift rates for western Oregon and along-strike variation in locking on the Cascadia subduction zone. *Journal of Geophysical Research: Solid Earth*, *114*(B1). https://doi.org/10.1029/2008jb005679

Byrnes, J. S., Toomey, D. R., Hooft, E. E. E., Nábělek, J., & Braunmiller, J. (2017). Mantle dynamics beneath the discrete and diffuse plate boundaries of the Juan de Fuca plate: Results from Cascadia Initiative body wave tomography. *Geochemistry, Geophysics, Geosystems*, *18*(8), 2906–2929. https://doi.org/10.1002/2017GC006980

Chaytor, J. D., Goldfinger, C., Dziak, R. P., & Fox, C. G. (2004). Active deformation of the Gorda plate: Constraining deformation models with new geophysical data. *Geology*, *32*(4), 353–356. https://doi.org/10.1130/G20178.2

Chen, C., Zhao, D., & Wu, S. (2015). Tomographic imaging of the Cascadia subduction zone: Constraints on the Juan de Fuca slab. *Tectonophysics*, *647*, 73–88. https://doi.org/10.1016/j.tecto.2015.02.012

Cloos, M. (1992). Thrust-type subduction-zone earthquakes and seamount asperities: A physical model for seismic rupture. *Geology*, *20*(7), 601. https://doi.org/10.1130/0091-7613(1992)020<0601:ttszea>2.3.co;2

Crotwell, H. P., Owens, T. J., & Ritsema, J. (1999). The TauP Toolkit: Flexible Seismic Travel-time and Ray-path Utilities. *Seismological Research Letters*, *70*(2), 154–160. https://doi.org/10.1785/gssrl.70.2.154

Dahlen, F. A., Hung, S.-H., & Nolet, G. (2000). Fréchet kernels for finite-frequency traveltimes-I. Theory. *Geophysical Journal International*, *141*(1), 157–174. https://doi.org/10.1046/j.1365-246X.2000.00070.x

Darold, A., & Humphreys, E. (2013). Upper mantle seismic structure beneath the Pacific northwest: A plume-triggered delamination origin for the Columbia river flood basalt eruptions. *Earth and Planetary Science Letters*, *365*, 232–242. https://doi.org/10.1016/j.epsl.2013.01.024

Delph, J. R., Levander, A., & Niu, F. (2018). Fluid controls on the heterogeneous seismic characteristics of the Cascadia margin. *Geophysical Research Letters*, *45*(20), 11021–11029. https://doi.org/10.1029/2018GL079518

Dijkstra, E. W. (1959). A note on two problems in connexion with graphs. *Numerische Mathematik*, *1*(1), 269–271. https://doi.org/10.1007/bf01386390

Divins, D. L. (2003). *Total sediment thickness of the world's oceans & marginal seas*. Boulder, CO: NOAA National Geophysical Data Center.

Dziewonski, A. M., & Anderson, D. L. (1983). Travel times and station corrections for P waves at teleseismic distances. *Journal of Geophysical Research*, *88*(B4), 3295. https://doi.org/10.1029/jb088ib04p03295

Eilon, Z. C., & Abers, G. A. (2017). High seismic attenuation at a mid-ocean ridge reveals the distribution of deep melt. *Science Advances*, *3*(5), e1602829. https://doi.org/10.1126/sciadv.1602829

Eilon, Z. C., & Forsyth, D. W. (2020). Depth-Dependent Azimuthal Anisotropy Beneath the Juan de Fuca Plate System. *Journal of Geophysical Research: Solid Earth*, *125*(8). https://doi.org/10.1029/2020jb019477

Furlong, K. P., & Schwartz, S. Y. (2004). Influence of the Mendocino triple junction on the tectonics of coastal California. *Annual Review of Earth and Planetary Sciences*, *32*(1), 403–433. https://doi.org/10.1146/annurev.earth.32.101802.120252

Gao, H. (2018). Three-dimensional variations of the slab geometry correlate with earthquake distributions at the Cascadia subduction system. *Nature Communications*, *9*(1). https://doi.org/10.1038/s41467-018-03655-5

Gardner, J. V., Cacchione, D. A., Drake, D. E., Edwards, B. D., Field, M. E., Hampton, M. A., et al. (1993). Map showing sediment isopachs in the deep-sea basins of the Pacific continental margin, Strait of Juan de Fuca to Cape Mendocino. In *U. S. Geological Survey Miscellaneous Investigations Series Map I-2091-A* (1 sheet, scale 1:1,000,000).

Geist, D., & Richards, M. (1993). Origin of the Columbia Plateau and Snake River plain: Deflection of the Yellowstone plume. *Geology*, *21*(9), 789. https://doi.org/10.1130/0091-7613(1993)021<0789:ootcpa>2.3.co;2

Hammond, W. C., & Humphreys, E. D. (2000). Upper mantle seismic wave velocity: Effects of realistic partial melt geometries. *Journal of Geophysical Research*, *105*(B5), 10975–10986. https://doi.org/10.1029/2000JB900041

Hammond, W. C., & Toomey, D. R. (2003). Seismic velocity anisotropy and heterogeneity beneath the mantle electromagnetic and tomography experiment (MELT) region of the east Pacific rise from analysis of P and S body waves. *Journal of Geophysical Research*, *108*(B4), 2176. https://doi.org/10.1029/2002jb001789

Haney, M. M., Power, J., West, M., & Michaels, P. (2012). Causal instrument corrections for short-period and broadband seismometers. *Seismological Research Letters*, *83*(5), 834–845. https://doi.org/10.1785/0220120031

Hawley, W. B., & Allen, R. M. (2019). The Fragmented Death of the Farallon Plate. *Geophysical Research Letters*, *46*(13), 7386–7394. https://doi.org/10.1029/2019gl083437

Hawley, W. B., Allen, R. M., & Richards, M. A. (2016). Tomography reveals buoyant asthenosphere accumulating beneath the Juan de Fuca plate. *Science*, *353*(6306), 1406–1408. https://doi.org/10.1126/science.aad8104

Jackson, D. D. (1979). The use of a priori data to resolve non-uniqueness in linear inversion. *Geophysical Journal International*, *57*(1), 137–157. https://doi.org/10.1111/j.1365-246X.1979.tb03777.x

James, D. E., Fouch, M. J., Carlson, R. W., & Roth, J. B. (2011). Slab fragmentation, edge flow and the origin of the Yellowstone hotspot track. *Earth and Planetary Science Letters*, *311*(1-2), 124–135.

Janiszewski, H. A., Gaherty, J. B., Abers, G. A., Gao, H., & Eilon, Z. C. (2019). Amphibious surface-wave phase-velocity measurements of the Cascadia subduction zone. *Geophysical Journal International*, *217*(3), 1929–1948. https://doi.org/10.1093/gji/ggz051

Kelsey, H. M., Engebretson, D. C., Mitchell, C. E., & Ticknor, R. L. (1994). Topographic form of the Coast Ranges of the Cascadia Margin in relation to coastal uplift rates and plate subduction. *Journal of Geophysical Research: Solid Earth*, *99*(B6), 12245–12255. https://doi.org/10.1029/93jb03236

Kennett, B. L. N., Engdahl, E. R., & Buland, R. (1995). Constraints on seismic velocities in the Earth from traveltimes. *Geophysical Journal International*, *122*(1), 108–124. https://doi.org/10.1111/j.1365-246X.1995.tb03540.x

Kuna, V. M., Nábělek, J. L., & Braunmiller, J. (2019). Mode of slip and crust–mantle interaction at oceanic transform faults. *Nature Geoscience*, *12*(2), 138–142. https://doi.org/10.1038/s41561-018-0287-1

Laske, G., Masters, G., Ma, Z., Pasyanos, M. E., & Livermore, L. (2013). Update on CRUST1.0: A 1-degree global model of Earth's crust. *Geophysical Research Abstracts*. https://igppweb.ucsd.edu/~gabi/rem.html

Leonard, L. J., Currie, C. A., Mazzotti, S., & Hyndman, R. D. (2010). Rupture area and displacement of past Cascadia great earthquakes from coastal coseismic subsidence. *Geological Society of America Bulletin*, *122*(11-12), 2079–2096. https://doi.org/10.1130/b30108.1

Lin, P. Y. P., Gaherty, J. B., Jin, G., Collins, J. A., Lizarralde, D., Evans, R. L., & Hirth, G. (2016). High-resolution seismic constraints on flow dynamics in the oceanic asthenosphere. *Nature*, *535*(7613), 538–541. https://doi.org/10.1038/nature18012

Littel, G. F., Thomas, A. M., & Baltay, A. S. (2018). Using Tectonic Tremor to Constrain Seismic Wave Attenuation in Cascadia. *Geophysical Research Letters*, *45*(18), 9579–9587. https://doi.org/10.1029/2018gl079344

Long, M. D. (2016). The Cascadia Paradox: Mantle flow and slab fragmentation in the Cascadia subduction system. *Journal of Geodynamics*, *102*, 151–170. https://doi.org/10.1016/j.jog.2016.09.006

Martin-Short, R., Allen, R. M., Bastow, I. D., Totten, E., & Richards, M. A. (2015). Mantle flow geometry from ridge to trench beneath the Gorda–Juan de Fuca plate system. *Nature Geoscience*, *8*(12), 1–21. https://doi.org/10.1038/ngeo2569

McCrory, P. A., Blair, J. L., Waldhauser, F., & Oppenheimer, D. H. (2012). Juan de Fuca slab geometry and its relation to Wadati-Benioff zone seismicity. *Journal of Geophysical Research*, *117*(9), 1–23. https://doi.org/10.1029/2012JB009407

Menke, W. (1985). *Geophysical data analysis: Discrete inverse theory*. Academic Press. https://doi.org/10.1016/C2011-0-69765-0

Moser, T. J. (1991). Shortest path calculation of seismic rays. *Geophysics*, *56*(1), 59–67. https://doi.org/10.1190/1.1442958

Obrebski, M., Allen, R. M., Xue, M., & Hung, S. H. (2010). Slab-plume interaction beneath the Pacific northwest. *Geophysical Research Letters*, *37*(14), 1–6. https://doi.org/10.1029/2010GL043489

Parsons, T., Blakely, R. J., Brocher, T. M., Christensen, N. I., Fisher, M. A., Flueh, E., et al. (2005). Crustal structure of the Cascadia fore arc of Washington. *U.S Geological Survey Professional Paper 1661-D*, Earthquake, 36. Retrieved from http://govreports.library.gatech.edu/handle/123456789/599

Portner, D. E., Beck, S., Zandt, G., & Scire, A. (2017). The nature of subslab slow velocity anomalies beneath South America. *Geophysical Research Letters*, *44*(10), 4747–4755. https://doi.org/10.1002/2017GL073106

Riddihough, R. P. (1980). Gorda plate motions from magnetic anomaly analysis. *Earth and Planetary Science Letters*, *51*(1), 163–170. https://doi.org/10.1016/0012-821X(80)90263-0

Riddihough, R. (1984). Recent movements of the Juan de Fuca plate system. *Journal of Geophysical Research*, *89*(B8), 6980–6994. https://doi.org/10.1029/JB089iB08p06980

Robertson, G. S., & Woodhouse, J. H. (1997). Comparison of P and station corrections and their relationship to upper mantle structure. *Journal of Geophysical Research: Solid Earth*, *102*(B12), 27355–27366. https://doi.org/10.1029/97jb02348

Roth, J. B., Fouch, M. J., James, D. E., & Carlson, R. W. (2008). Three-dimensional seismic velocity structure of the northwestern United States. *Geophysical Research Letters*, *35*(15), 1–6. https://doi.org/10.1029/2008GL034669

Ruan, Y., Forsyth, D. W., & Bell, S. W. (2014). Marine sediment shear velocity structure from the ratio of displacement to pressure of Rayleigh waves at seafloor. *Journal of Geophysical Research: Solid Earth*, *119*(8), 6357–6371. https://doi.org/10.1002/2014jb011162

Ruff, L. J. (1989). Do trench sediments affect great earthquake occurrence in subduction zones? *Pure and Applied Geophysics PAGEOPH*, *129*(1–2), 263–282. https://doi.org/10.1007/BF00874629

Rychert, C. A., Harmon, N., & Tharimena, S. (2018). Scattered wave imaging of the oceanic plate in cascadia. *Science Advances*. https://doi.org/10.1126/sciadv.aao1908

Schmalzle, G. M., McCaffrey, R., & Creager, K. C. (2014). Central Cascadia subduction zone creep. *Geochemistry, Geophysics, Geosystems*, *15*(4), 1515–1532. https://doi.org/10.1002/2013GC005172

Schmandt, B., Dueker, K., Humphreys, E., & Hansen, S. (2012). Hot mantle upwelling across the 660 beneath Yellowstone. *Earth and Planetary Science Letters*, *331–332*, 224–236. https://doi.org/10.1016/j.epsl.2012.03.025

Schmandt, B., & Humphreys, E. (2010a). Complex subduction and small-scale convection revealed by body-wave tomography of the western United States upper mantle. *Earth and Planetary Science Letters*, *297*(3–4), 435–445. https://doi.org/10.1016/j.epsl.2010.06.047

Schmandt, B., & Humphreys, E. (2010b). Seismic heterogeneity and small-scale convection in the southern California upper mantle. *Geochemistry, Geophysics, Geosystems*, *11*(5), 1–19. https://doi.org/10.1029/2010GC003042

Schmandt, B., & Humphreys, E. (2011). Seismically imaged relict slab from the 55 Ma Siletzia accretion to the northwest United States. *Geology*, *39*(2), 175–178. https://doi.org/10.1130/G31558.1

Schmandt, B., & Lin, F. (2014). P and S wave tomography of the mantle beneath the United States. *Geophysical Research Letters*, *41*(18), 6342–6349. https://doi.org/10.1002/2014GL061231

Shaw, P. R., & Orcutt, J. A. (1985). Waveform inversion of seismic refraction data and applications to young Pacific crust. *Geophysical Journal International*, *82*(3), 375–414. https://doi.org/10.1111/j.1365-246x.1985.tb05143.x

Sigloch, K., McQuarrie, N., & Nolet, G. (2008). Two-stage subduction history under North America inferred from multiple-frequency tomography. *Nature Geoscience*, *1*(7), 458–462. https://doi.org/10.1038/ngeo231

Small, C., & Danyushevsky, L. V. (2003). Plate-kinematic explanation for mid-oceanic-ridge depth discontinuities. *Geology*, *31*(5), 399. https://doi.org/10.1130/0091-7613(2003)031<0399:pefmdd>2.0.co;2

Stanciu, A. C., & Humphreys, E. D. (2020). Upper mantle tomography beneath the Pacific Northwest interior. *Earth and Planetary Science Letters*, *539*, 116214. https://doi.org/10.1016/j.epsl.2020.116214

Stern, R. J. (2002). Subduction zones. *Reviews of Geophysics*, *40*(4). https://doi.org/10.1029/2001rg000108

Stock, J. M., & Lee, J. (1994). Leave a geological record? *America*, *13*(6), 1472–1487.

Tarantola, A., & Valette, B. (1982). Generalized nonlinear inverse problems solved using the least squares criterion. *Reviews of Geophysics*, *20*(2), 219. https://doi.org/10.1029/RG020i002p00219

Tian, Y., & Zhao, D. (2012). P-wave tomography of the western United States: Insight into the Yellowstone hotspot and the Juan de Fuca slab. *Physics of the Earth and Planetary Interiors*, *200*, 72–84.

Toomey, D. R., Allen, R., Barclay, A., Bell, S., Bromirski, P., Carlson, R., et al. (2014). The Cascadia initiative: A sea change in seismological studies of subduction zones. *Oceanography*, *27*(2), 138–150. https://doi.org/10.5670/oceanog.2014.49

Toomey, D. R., Solomon, S. C., & Purdy, G. M. (1994). Tomographic imaging of the shallow crustal structure of the East Pacific Rise at 9°30′N. *Journal of Geophysical Research*, *99*(B12), 24135–24157. https://doi.org/10.1029/94jb01942

Trehu, A. M., Asudeh, I., Brocher, T. M., Luetgert, J. H., Mooney, W. D., Nabelek, J. L., & Nakamura, Y. (1994). Crustal architecture of the cascadia forearc. *Science*, *266*(5183), 237–243. https://doi.org/10.1126/science.266.5183.237

VanDecar, J. C., & Crosson, R. S. (1990). Determination of teleseismic relative phase arrival times using multi-channel cross-correlation and least squares. *Bulletin of the Seismological Society of America*, *80*(1), 150–169. Retrieved from http://www.bssaonline.org/content/80/1/150.short

VanderBeek, B. P., & Toomey, D. R. (2017). Shallow Mantle Anisotropy Beneath the Juan de Fuca Plate. *Geophysical Research Letters*, *44*(22), 11,382–11,389. https://doi.org/10.1002/2017gl074769

VanderBeek, B. P., & Toomey, D. R. (2019). Pn Tomography of the Juan de Fuca and Gorda Plates: Implications for Mantle Deformation and Hydration in the Oceanic Lithosphere. *Journal of Geophysical Research: Solid Earth*, *124*(8), 8565–8583. https://doi.org/10.1029/2019jb017707

VanderBeek, B., & Faccenda, M. (2020). Can Teleseismic Travel-Times Constrain 3D Anisotropic Structure in Subduction Zones? Insights from Realistic Synthetic Experiments. *EGU General Assembly Conference Abstracts*, (14886).

Wada, I., Mazzotti, S., & Wang, K. (2010). Intraslab Stresses in the Cascadia Subduction Zone from Inversion of Earthquake Focal Mechanisms. *Bulletin of the Seismological Society of America*, *100*(5A), 2002–2013. https://doi.org/10.1785/0120090349

Waldhauser, F., Lippitsch, R., Kissling, E., & Ansorge, J. (2002). High-resolution teleseismic tomography of upper-mantle structure using an a priori three-dimensional crustal model. *Geophysical Journal International*, *150*(2), 403–414. https://doi.org/10.1046/j.1365-246X.2002.01690.x

Wells, R. E., Blakely, R. J., Wech, A. G., McCrory, P. A., & Michael, A. (2017). Cascadia subduction tremor muted by crustal faults. *Geology*, *45*(6), 515–518. https://doi.org/10.1130/G38835.1

Wilson, D. S. (1986). A kinematic model for the Gorda deformation zone as a diffuse southern boundary of the Juan de Fuca plate. *Journal of Geophysical Research*, *91*(B10), 10259. https://doi.org/10.1029/jb091ib10p10259

Wilson, D. S. (1989). Deformation of the so-called Gorda Plate. *Journal of Geophysical Research: Solid Earth*, *94*(B3), 3065–3075. https://doi.org/10.1029/jb094ib03p03065